Society of Medical Education & Research

2022, Volume 2, Issue 1, Page No: 117-142
ISSN: 3108-4826

Journal of Medical Sciences and Interdisciplinary Research

NRP2-Dependent Migrasomal Signaling Drives Pro-Efferocytic Macrophage Polarization in Colorectal Cancer Liver Metastasis

Daniel Victor Alvarez[1], Miguel Angel Soto[1]*, Ricardo Tomas Perez[2], Juan Sebastian Molina[2], Andres Felipe Rojas[3], Esteban Nicolas Castro[3]

[1]Department of Management, Universidad de los Andes, Bogotá, Colombia.
[2]Facultad de Administración, Universidad Nacional de Colombia, Bogotá, Colombia.
[3]School of Business, Universidad EAFIT, Medellín, Colombia.

***E-mail** ✉ m.soto.uniandes@yahoo.com

Abstract

Migrasomes represent an emerging category of extracellular vesicles, but their contribution to metastasis in colorectal cancer (CRC) is not well elucidated. The present research sought to examine the role of migrasomes originating from CRC cells, especially in low-oxygen environments, in driving spread to the liver and altering the immune landscape within tumors.The presence of migrasomes in CRC samples and cell lines was assessed through transmission electron microscopy and immunofluorescence techniques. Functional effects and cell-to-cell interactions were investigated using a murine model of liver metastasis along with single-cell RNA sequencing (scRNA-seq).Migrasome formations were detected in both original CRC tumors and liver metastatic sites. Real-time imaging of living cells showed that CRC cells in hypoxia produced higher quantities of migrasomes. In animal studies, migrasomes from hypoxic conditions accumulated in the liver and accelerated metastatic development there. Analysis via scRNA-seq on liver metastatic lesions indicated that these migrasomes reshaped the tumor ecosystem, particularly by increasing a population of Tmem45a$^+$ fibroblasts displaying myofibroblast characteristics and fostering the development of CD5L$^+$ macrophages with enhanced ability to engulf dying cells. At the molecular level, NRP2, which is abundant in migrasomes from hypoxic CRC cells, was delivered to macrophages, where it interacted with PROX1 to stimulate CD5L production and enhance receptors involved in efferocytosis. Reducing NRP2 expression in CRC cells prevented the migrasome-driven shift toward CD5L$^+$ macrophages and reduced the removal of apoptotic cancer cells.This work illustrates how migrasomes released by hypoxic CRC cells support liver spread by modifying stromal and immune elements, mainly via NRP2/PROX1-directed reprogramming of macrophages into a CD5L$^+$ state that favors efferocytosis. The results uncover a novel pathway of cell-to-cell signaling through migrasomes during CRC advancement and suggest a promising target for treating metastatic cases.

Keywords: Hypoxia-induced migrasome, Liver metastasis in colorectal cancer, Efferocytosis by macrophages, CD5L$^+$

Introduction

Spread to the liver is the primary reason for death associated with colorectal cancer (CRC), representing 70% of metastatic instances in this disease. Although progress has been made in detection and treatment methods, outcomes for individuals with liver involvement from CRC continue to be unfavorable, featuring a 5-year survival of only 30% [1]. Emerging evidence indicates that the effective seeding of CRC cells in the liver involves more than physical movement, relying heavily on targeted interactions between tumor cells and immune components in the surrounding environment [2]. Thus, pinpointing critical factors that enable dialogue between malignant cells and immune

Access this article online https://smerpub.com/

Received: 05 February 2022; **Accepted:** 29 April 2022

How to cite this article: Alvarez DV, Soto MA, Perez RT, Molina JS, Rojas AF, Castro EN. NRP2-Dependent Migrasomal Signaling Drives Pro-Efferocytic Macrophage Polarization in Colorectal Cancer Liver Metastasis. J Med Sci Interdiscip Res. 2022;2(1):117-42. https://doi.org/10.51847/Z6oxsHzvgl

players, as well as clarifying how such exchanges promote liver metastasis in CRC, is essential for creating innovative treatments and enhancing patient outcomes.

Migrasomes constitute a newly identified form of extracellular vesicle that offers a fresh avenue for communication between cells and the sideways movement of intracellular materials [3, 4]. In contrast to typical extracellular vesicles, migrasomes possess distinct processes for formation, content loading, movement, and impact on target cells. Their development requires cellular movement and takes place at the ends or junctions of retraction fibers, with sizes between 0.5 and 3 μm and a characteristic pomegranate-like appearance. Intracellular elements such as mitochondria, mRNA, and proteins may be selectively directed into migrasomes; upon retraction fiber rupture, these vesicles detach from the originating cell and are absorbed by nearby cells [5]. In this way, migrasomes enable the transfer of substances and signaling across cells. Known markers for migrasomes include TSPAN4, integrins, NDST1, PIGK, CPQ, and EOGT [6]. Growing data point to migrasome involvement in maintaining mitochondrial integrity [7], blood vessel formation [8], and tissue development [9], alongside contributions to disorders like heart conditions, neurological diseases, and malignancies. For example, migrasomes from neutrophils contain adhesion proteins and clotting components, enabling preferential buildup at damaged areas to activate platelets and initiate coagulation [10]. In cerebral amyloid angiopathy cases, macrophages generate more migrasomes carrying CD5L, which attaches to blood vessels and reduces tolerance to complement attack [11]. Migrasomes from glioblastoma transport autophagosomes and ease stress on the endoplasmic reticulum [12]. Notably, accumulating reports show that migrasomes or exosomes from tumors can advance metastatic spread. Examples include tumor exosomal miR-934 [13] and HSPC111 [14] aiding CRC liver metastasis. Breast cancer migrasomes facilitate tumor-osteoclast crosstalk, generating osteoclast variants linked to bone spread [15]. Migrasomes rich in CD151 drive hepatocellular carcinoma progression through enhanced vessel growth [16]. In prior work from our group, we described how extracellular vesicles like exosomes allow natural killer cells to influence immune escape in CRC [17]. Yet, the potential involvement of migrasomes, this distinct extracellular vesicle type, in immune modulation and CRC liver metastasis remains uninvestigated.

Efferocytosis refers to the mechanism through which phagocytes accurately detect and internalize nearby dying cells, contributing significantly to immunosuppression. Macrophages serve as primary effectors capable of repeatedly clearing apoptotic bodies via sustained efferocytosis [18]. The process involves three main phases [19, 20]: Recruitment, in which dying cells emit “find-me” cues like CX3CL1, ATP, and RPS19 to attract phagocytes through chemotaxis; Binding, where phagocytes identify exposed phosphatidylserine on apoptotic cells either directly (via receptors such as BAI1 or TIM1) or indirectly (through bridges involving AXL or MerTK); and Ingestion followed by intracellular degradation in lysosomes. Mounting data indicate that efferocytosis by macrophages fosters an immunosuppressive setting within tumors, allowing malignant cells to escape detection by the immune system. For example, clearance of dying breast tumor cells by macrophages boosts the release of suppressive cytokines and recruitment of myeloid suppressor cells, leading to reduced immunity and increased metastatic potential [21]. In colorectal cancer (CRC), this process creates conditions favoring M2-like macrophages, suppressing immunity by dampening STING/IFN-I pathways and lowering cytotoxic T-cell function [22]. Targeted inhibition of the efferocytosis receptor MerTK has been shown to restrict tumor expansion in models of CRC liver spread [23]. Collectively, these observations highlight macrophage efferocytosis as a central factor in establishing immunosuppression and facilitating metastasis. Nevertheless, it is unclear if migrasomes influence macrophage efferocytosis and thus contribute to liver metastasis in CRC.

The current work sought to determine if hypoxic CRC cells enhance liver colonization by releasing migrasomes that specifically boost efferocytosis within distinct macrophage subsets. Accordingly, we initially confirmed migrasome occurrence in patient-derived CRC liver metastases and cultured CRC lines. Using single-cell RNA sequencing (scRNA-seq) analysis, we identified $CD5L^+$ macrophages as the chief targets of tumor-sourced migrasomes. We then performed comprehensive functional experiments both in living organisms and cultured systems, combined with molecular studies, to clarify how migrasomes from hypoxic CRC cells govern the emergence of $CD5L^+$ macrophages and their capacity for efferocytosis. These results offer fresh perspectives on how cancer-released migrasomes remodel the immune

landscape during metastasis and reveal a novel pathway underlying CRC spread to the liver.

Materials and Methods

Tumor samples

Primary colorectal tumors (n = 3), liver metastases from CRC (n = 3), and matched normal adjacent tissues (n = 3) were obtained from Shenzhen Longhua District Central Hospital under approval by the hospital's Institutional Review Board (IRB) (2024-049-02). Informed written consent was secured from every participant, patient privacy was protected, and all protocols complied with the Declaration of Helsinki. Enrollment required: (1) confirmed CRC diagnosis via pathology; (2) surgical resection planned; (3) absence of prior cancers or conditions impairing immunity. Patients were excluded if they had: (1) received neoadjuvant chemo- or radiotherapy; (2) autoimmune diseases or active severe infections; (3) missing clinical/pathological records. Specimens were harvested surgically and promptly snap-frozen in liquid nitrogen or fixed in formalin for later use. Age and gender distributions were comparable among groups.

Isolation and culture of primary CRC cells from tumor specimens

Primary colorectal cancer cells were derived from fresh surgical specimens employing the Tumor Dissociation Kit, Human (#130-095-929, Miltenyi). In short, tumor pieces were washed in ice-cold PBS and chopped into 2–4 mm pieces. Digestion proceeded by adding 5 mL of kit-prepared enzyme mix to 4.4 mL RPMI 1640 medium, followed by incubation at 37 °C with agitation (75 rpm, 5% CO_2) for 30 min. The digest was gently disrupted by pipetting with a wide-tip pipette (10 cycles) and passed through a 70 µm filter. Cells were pelleted by centrifugation (250 × g, 3 min, 4 °C) and resuspended in complete medium (RPMI 1640 plus 10% FBS and 1% penicillin-streptomycin).

Transmission Electron Microscopy (TEM)

TEM served to visualize the migrasome ultrastructure. Samples were promptly fixed in glutaraldehyde, post-fixed in osmium tetroxide, dehydrated in ascending ethanol concentrations (30%, 50%, 70%, 90%, and 100%), and embedded in resin. Embedded blocks were sectioned to 50–100 nm thickness on an ultramicrotome. Sections were placed on copper grids, negatively stained with phosphotungstic acid, and examined using a TEM instrument (JEM-1200EX, Japan Electronics Co., LTD) for image acquisition.

Immunofluorescence (IF)

Sections or cells were fixed in 4% paraformaldehyde, permeabilized using Triton X-100, and blocked with 5% BSA. Incubation occurred with primary antibodies: CD5L (1:500, 17224-1-AP, Proteintech), CD163 (1:200, ab182422, Abcam), NRP2 (1:250, #3366, CST), PROX1 (1:250, sc-81983, Santa Cruz), MERTK (200 µg/mL, sc-365499, Santa Cruz). After removal of unbound primaries, fluorochrome-labeled secondary antibodies were applied. Samples were washed, counterstained with DAPI-containing mounting medium, and viewed under fluorescence microscopy.

Cell culture, hypoxic treatment, and transfection

Human CRC lines P53R (#iCell-h169) and HCT116 (#iCell-h071) were acquired from iCell Bioscience Inc, as were murine lines CT26 (#iCell-m014) and MC38 (#iCell-m032). HCT116 cells were grown in McCoy's 5 A medium, CT26 in RPMI-1640, while P53R and MC38 were maintained in Dulbecco's Modified Eagle Medium (DMEM). All media contained 10% fetal bovine serum (FBS, 10099-141, GIBCO), 1% penicillin-streptomycin (P/S, E607011, Sangon), 1% non-essential amino acid (iCell-01000, iCell), 1% sodium pyruvate (iCell-01100, iCell), 1% HEPES (iCell-01200, iCell), and 1% GlutaMAX-1 (iCell-0900, iCell).

To assess the impact of low-oxygen conditions on colorectal cancer (CRC) cells, cultures were maintained in a hypoxic environment (1% O_2, 5% CO_2, 94% N_2) at 37 °C within a tri-gas incubator (Thermo Scientific) for 24 h. Corresponding normoxic samples were kept in a conventional incubator with 5% CO_2 at 37 °C over the identical period.

Murine bone marrow-derived macrophages (BMDMs) were employed throughout this investigation. Isolation involved harvesting femurs and tibias, followed by meticulous removal of surrounding tissue. The epiphyses at both ends were severed with sterile scissors. Ice-cold high-glucose DMEM was loaded into a 1–2 mL syringe and used to repeatedly flush the marrow cavity (at least three times) until the bone appeared white and devoid of red hue. The expelled cell suspension was vigorously pipetted to break up aggregates, then filtered through a 200-mesh strainer to eliminate debris. Filtered cells were collected in a 15 mL tube, spun at 300 × g for 5 min, and

the pellet was resuspended in chilled specialized medium for BMDM culture (iCell-i017-002 m, CytoSci Biosciences).

Stable NRP2 knockdown in MC38 cells was achieved via lentiviral transduction using pSlenti-U6-shRNA (NRP2)-CMV-F2A-Puro-WRPE constructs. Lentiviruses were produced in HEK293T cells through a conventional three-plasmid packaging protocol, with viral supernatant collected 48–72 h after transfection. The supernatant was passed through a 0.45 μm filter and added to MC38 cultures supplemented with 8 μg/mL polybrene to improve transduction. At 48 h post-exposure, puromycin selection (2 μg/mL) was applied for 3–5 days to enrich transduced populations.

For NRP2 overexpression, the full-length NRP2 coding region was inserted into pcDNA3.1, and the resulting plasmid was introduced into BMDMs via Lipofectamine 2000 (#11668019, Invitrogen). Transient silencing of NRP2, PROX1, and MERTK was performed by transfecting specific siRNAs into BMDMs with Lipofectamine 2000 following the supplier's protocol. Culture medium was refreshed 6 h after transfection, and cells were collected 24 h later**.**

Migrasomes isolation

Migrasome purification followed the protocol outlined by Gu *et al*. [24]. In brief, after 48 h of culture, cells were exposed to 5 μg/mL cytochalasin B for 30 min to facilitate migrasome release. Cells were then trypsinized to form a suspension, which was centrifuged at 500 × g for 5 min. The resulting supernatant was layered over a discontinuous Ficoll gradient (5%, 10%, 15%, and 25%) and subjected to ultracentrifugation at 150,000 × g for 60 min. The migrasome-enriched fraction was recovered by careful aspiration of the interface between the 15% and 25% layers.

Live-cell migrasome labeling and visualization

For real-time observation of migrasomes in CRC cells, cultures were stained with Wheat Germ Agglutinin-Alexa Fluor 488 conjugate (WGA-488, Cat# W11261, Thermo Fisher Scientific) at a 1:500 dilution. Incubation occurred at room temperature in darkness for 10 min, after which immediate imaging was conducted using live-cell fluorescence microscopy.

Additionally, to track migrasomes dynamically, TSPAN4 was fused to GFP and subcloned into an expression vector. CRC cells were transfected with the TSPAN4-GFP construct using Lipofectamine 2000, and GFP-positive migrasomes were monitored via fluorescence microscopy in living cells.

Western Blot (WB)

Protein extracts from tissues or cells were prepared by lysis, quantified using the BCA assay kit (Thermo Scientific, USA), and resolved on 10% SDS-PAGE gels. Resolved proteins were electrotransferred to PVDF membranes, which were then blocked with 5% nonfat milk to prevent nonspecific binding. Membranes were probed overnight at 4 °C with primary antibodies against NRP2 (1:1000, Proteintech, 27193-1-AP), CALR (1:1000, Proteintech, 10292-1-AP), PIGK (1:1000, Proteintech, 15151-1-AP), CPQ (1:1000, Proteintech, 16601-1-AP), EOGT (1:1500, Proteintech, 27595-1-AP), CD63 (1:1000, Proteintech, 25682-1-AP), TSG101 (1:5000, Abcam, ab125011), CD9 (1:3000, Proteintech, 20597-1-AP), PROX1 (1:500, Santa Cruz, sc-81983), and GAPDH (1:1000, Proteintech, 60004-1-Lg). Secondary incubation employed HRP-conjugated goat anti-rabbit IgG (H + L) (1:5000, Proteintech, SA00001-2) for 1 h at room temperature. After thorough washing, signals were developed and captured using a chemiluminescence imaging system (Qinxiang, Shanghai, China).

Mice treatment

Sixteen C57BL/6J mice aged 4–6 weeks were obtained from Junke Biology (CSXK(Zhe)2019-0004). Animals were maintained in a controlled facility at 24–26 °C, 55–60% humidity, under a 12-hour light/dark cycle, with unrestricted access to water. A 7-day acclimation period preceded experimental procedures.

All animal studies received approval from the Laboratory Animal Ethics Committee of Guangdong Medical University (GDY2402433).

To examine migrasome biodistribution in vivo, six mice were allocated randomly to two groups and administered tail-vein injections of DiR-labeled migrasomes derived from normoxic (Nor-Mig) or hypoxic (Hyp-Mig) conditions. Whole-body fluorescence imaging was performed 3 h post-injection.

A model of CRC liver metastasis was generated to evaluate migrasome-specific influences. Ten mice were randomized into groups, weighed, and anesthetized with avertin. After skin sterilization, a small longitudinal incision (~ 0.5 cm) was made below the left costal margin to access the spleen. A 0.2 mL suspension of MC38 cells was intrasplenically injected. Migrasomes (50 μg) from

MC38 cultures were delivered intravenously every 3 days. On day 14, bioluminescence imaging assessed hepatic metastases. Animals were humanely euthanized by CO_2 overdose, and livers were harvested for macroscopic counting of metastatic nodules.

Single-cell RNA sequencing (scRNA-seq) procedure

Tumor specimens were obtained from MC38-bearing mice administered migrasomes isolated from MC38 cultures maintained in either standard oxygen or low-oxygen settings, using one specimen per condition. Cell density was standardized to 1×10^6 cells/mL. Shortly after preparing the suspension (within 15 min), cells were encapsulated in GemCode beads and loaded onto chips as directed by the protocol. Emulsions were processed on the Chromium™ Controller (Pleasanton, California) for lysis and cDNA synthesis. Libraries were built with the 10x Genomics kit (MobiDrop, China) and run on the Illumina NextSeq500 sequencer according to guidelines. Each library exceeded 100 million reads, yielding roughly 30,000 reads per cell on average.

Processing of scRNA-seq datasets

Read alignment and quantification were handled via MobiDrop's MobiVision tool. Downstream filtering and analysis utilized Seurat (R package version 4.3.0.1). Retained cells fulfilled these standards: UMI counts ranging 500–100,000; gene detection 200–9,000; mitochondrial transcripts under 25%; and erythrocyte markers under 3%. Genes appearing in fewer than three cells were discarded. Doublets were excluded after detection with DoubletFinder (version 2.0.4). Integration to mitigate batch effects employed Seurat's built-in functions. Reduction to lower dimensions proceeded through PCA, then UMAP for 2D visualization. Clustering relied on SNN modality informed by PCA outcomes. Preliminary cell typing used SingleR against BlueprintEncodeData, followed by manual adjustment with canonical markers for definitive identities. Cluster-specific DEGs were found via FindAllMarkers, while group comparisons used FindMarkers. Significance required $|\log_2 FC| > 1$ alongside Bonferroni-adjusted $p < 0.05$. Interactions across cell populations were inferred through CellPhoneDB.

A collection of 341 efferocytosis-associated genes was generated by merging relevant pathways from KEGG and MSigDB resources. Separately, 23 migrasome-associated genes were selected based on prior reports. Per-sample enrichment scores for both pathways were derived using ssGSEA from the GSVA package (version 1.46.0). Group comparisons were displayed as paired boxplots via ggplot2, with differences tested by the Wilcoxon method.

Isolation via flow cytometry

Macrophages expressing CD5L were purified through sorting. Murine bone marrow-derived macrophages were differentiated over 6 days in macrophage-specific medium (iCell-i017-002 m, CytoSci Biosciences) containing 100 ng/mL M-CSF (91109ES10, Yeasen). On day 6, cells were released first with 12 mM lidocaine (HY-B0185A, MCE) for 3 min, then a brief trypsin treatment for another 3 min. Suspension was achieved by pipetting, followed by pelleting at 300 × g (3 min) and resuspension in 1 mL PBS. Density was set to 1×10^7 cells/tube, centrifuged at 350 × g (5 min), and resuspended in 200 µL buffer (2% FBS/PBS). Primary staining used 0.5 µg CD5L antibody (BAF2834, R&D Systems) for 60 min at 4 °C protected from light. After one PBS wash and spin (350 × g, 5 min), secondary staining was applied using 0.25 µL anti-goat IgG (Alexa 488-conjugated, 1:1000, ab150129, Abcam) for 30 min at 4 °C in the dark. A final wash (1 mL buffer, 200 × g, 3 min) preceded resuspension in sorting medium (5 mM EDTA, 10 mM HEPES, 2% FBS/PBS) and analysis on FACSVerse™ (BD Biosciences).

Phagocytosis assay in macrophages

Effects of low-oxygen migrasomes on engulfment were tested by exposing BMDMs to 100 µg/mL migrasomes from either oxygen condition for 48 h (PBS as control). MC38 targets were marked with 1 µg/mL propidium iodide (PI, IP5030, Solarbio) to highlight dying cells, pelleted (1000 × g, 5 min), and added to treated macrophages for 24 h co-culture. Samples were then fixed (4% paraformaldehyde, 30 min, room temperature), permeabilized (0.3% Triton X-100, 15 min), and blocked (3% BSA, 30 min). Overnight incubation at 4 °C with F4/80 antibody (1:200, 28463-1-AP, Proteintech) was followed by 1 h secondary (1:500, ab150077, Abcam) at room temperature away from light. DAPI staining (10 min, dark) enabled nuclear visualization under fluorescence microscopy.

Migrasome staining and NRP2-GFP localization

NRP2 association with migrasomes was probed by fusing its coding region to GFP in a plasmid, then transfecting hypoxic MC38 cells with Lipofectamine™ 2000

(Invitrogen, USA) per instructions. Medium change occurred after 6 h, with further incubation for 48 h before the migrasome harvest.

Isolated migrasomes were marked using DiI red dye (C1036, Beyotime, China) via routine labeling. Free dye was cleared by PBS rinses and high-speed spin (20,000 × g, 1 h, 4 °C); pellet was redissolved in PBS. Labeled migrasomes were added to BMDMs for overnight uptake at 37 °C with mild agitation. Hoechst 33,342 (C1029, Beyotime, China) provided nuclear contrast (10 min, room temperature, dark) prior to fluorescence imaging.

Co-immunoprecipitation procedure

Cells were rinsed twice in chilled PBS, harvested by scraping, and spun at 800 × g (5 min, 4 °C). Lysis employed 1 mL Pierce buffer (87787, Thermo Fisher) plus protease (78438) and phosphatase (78426) inhibitors for 30 min on ice. Debris was removed by spinning (13,000 rpm, 15 min, 4 °C). RNA degradation used RNase A/T1 (EN0551, Thermo Fisher) for 30 min at room temperature. Input retained 10% volume. Remaining material was precleared with 25 µL Protein A/G beads (88803, Thermo Fisher) for 1 h at 4 °C. Immunoprecipitation proceeded overnight at 4 °C with 2.5 µg NRP2 antibody (CST #3366), then 4 h bead binding at 4 °C. Triple washes (5 min each) used buffer containing 10 mM Tris-HCl (pH 7.5), 1 mM EDTA, 1 mM EGTA, 150 mM NaCl, 1% Triton X-100, and 0.2 mM sodium orthovanadate. Elution involved heating in 1× loading buffer (95 °C, 10 min) before western blot analysis.

RT-qPCR procedure

Total RNA was converted to cDNA using a reverse transcription kit (#K1622, Thermo), after which quantitative PCR was carried out with 2×Master Mix (Roche) on the ABI Q6 platform (Applied Biosystems). Gene expression levels relative to control were calculated via the $2^{-\Delta\Delta Ct}$ approach, with normalization against GAPDH.

Enzyme-linked immunosorbent assays (ELISA)

Concentrations of murine TGF-β, IL-10, and CCL2 were determined with dedicated commercial ELISA kits following the supplied instructions. TGF-β measurement employed the Mouse TGF-β ELISA kit (ML057830, Enzyme-linked Biology), IL-10 used the Mouse IL-10 ELISA kit (ML037873, Enzyme-linked Biology), and CCL2 utilized the Mouse MCP-1/CCL2 ELISA kit (ML037840, Enzyme-linked Biology).

Transwell migration and invasion experiments

The influence of NRP2 overexpression or MERTK silencing in macrophages on the migratory capacity of CFSE-stained colorectal cancer (CRC) cells was assessed through a Transwell co-culture system. Modified bone marrow-derived macrophages (BMDMs) were prepared at 1×10^5 cells/mL. MC38 cells were stained with CFSE (ab113853, Abcam), then transferred to serum-free medium at 1×10^5 cells/mL. Each lower chamber (24-well format) received 700 µL of complete MC38 medium supplemented with 10% FBS. The upper insert was loaded with 500 µL total volume comprising equal parts (250 µL each) of BMDM suspension and CFSE-labeled MC38 cells, followed by 48 h incubation in a CO_2-controlled environment. Post-incubation, inserts were removed, upper-chamber medium aspirated, and non-migrated cells on the top membrane surface gently cleared using a damp cotton swab. Cells that had transmigrated to the bottom surface were examined via fluorescence microscopy.

To explore paracrine regulation of CRC cell movement and invasion by macrophages independent of efferocytosis, conditioned medium (CM) was harvested from macrophages under efferocytosis-blocked conditions and applied to CRC cells in separate Transwell setups. Four experimental groups were established: blank CM (from $CD5L^-$ macrophages exposed to untreated apoptotic MC38 cells), $CD5L^+$ CM (from $CD5L^+$ macrophages exposed to untreated apoptotic MC38 cells), blocked $CD5L^+$ CM (from $CD5L^+$ macrophages exposed to Annexin V–pretreated apoptotic MC38 cells), and hypoxic migrasome-treated blocked $CD5L^+$ CM (from $CD5L^+$ macrophages exposed to Annexin V–pretreated apoptotic MC38 cells plus 100 µg/mL hypoxic migrasomes). All macrophage cultures were maintained in serum-free conditions. Efferocytosis blockade involved pre-incubation of apoptotic MC38 cells with 3 µg/mL Annexin V (abbkine, PRP3003), whereas untreated apoptotic cells served as positive controls. Following 48 h of co-culture per group, supernatants were harvested as CM. In the subsequent Transwell setup, lower chambers contained 700 µL complete MC38 medium with 10% FBS, while upper chambers received 500 µL total comprising equal volumes (250 µL each) of CM and MC38 suspension, incubated for 48 h under CO_2 control. Transmigrated or invaded cells were detected and counted by fluorescence

microscopy. Standard migration used 8.0 µm pore 24-well inserts (353097, FALCON), while invasion employed equivalent Matrigel-precoated inserts (354480, FALCON).

Data statistics

All statistical evaluations were conducted in GraphPad version 10.0. Comparisons involving three or more groups employed two-tailed ANOVA with Tukey's post-hoc correction. Pairwise comparisons used a two-tailed Student's t-test. Differences achieving $p < 0.05$ were deemed statistically significant.

Results and Discussion

Detection of migrasomes originating from colorectal cancer cells

Research on migrasomes within the tumor context remains preliminary, with no prior documentation of their involvement in tumor immune responses or CRC progression. Accordingly, our initial objective was to verify the existence of migrasomes in CRC tumor samples. Transmission electron microscopy (TEM) was applied to ultrathin sections prepared from patient-derived normal adjacent tissue, primary non-metastatic CRC tumors, and liver metastases from CRC cases. Across all specimens, we identified abundant oval vesicles resembling pomegranates, sized 0.5 to 3.0 µm, either connected to retracted retraction fibers or released into extracellular spaces following membrane rupture **(Figure 1a)**, aligning closely with established migrasome characteristics [5]. Migrasomes were thus confirmed in the tumor milieu, exhibiting notably higher abundance in liver metastatic samples **(Figure 1b)**. These observations establish the occurrence of migrasomes in CRC tissues and suggest a potential link to hepatic metastasis.

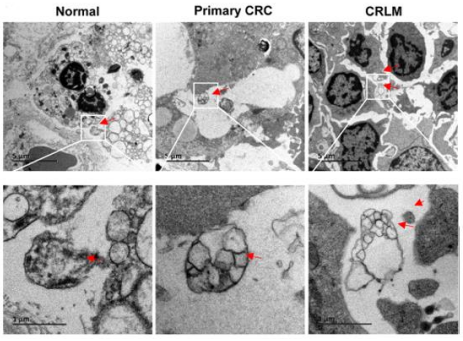

a)

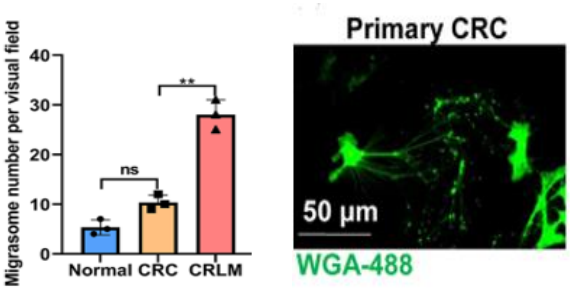

b) c)

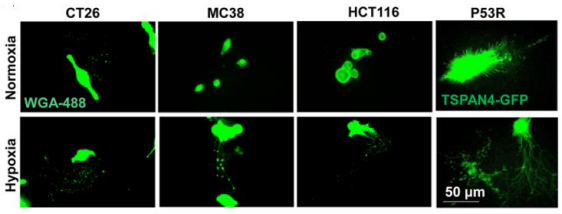

d)

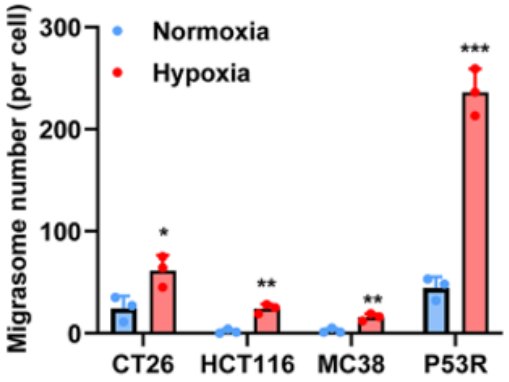

e)

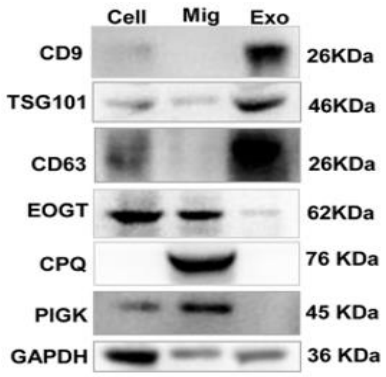

f)

Figure 1. Detection of migrasomes originating from colorectal cancer (CRC) cells. (a) Transmission electron micrographs displaying vesicle structures resembling migrasomes (marked by red arrows) in

tissues adjacent to tumors, primary CRC samples, and liver metastases from CRC patients. (b) Counts of migrasomes per microscopic field derived from images in panel (a). (c) Time-lapse observation of primary CRC cells stained with WGA-488, illustrating the process of migrasome generation. (d) Typical micrographs of WGA-488-stained migrasomes in CT26, HCT116, and MC38 cell lines grown in either standard oxygen or low-oxygen environments, alongside TSPAN4-GFP-tagged migrasomes in P53R cells. (e) Measurement of migrasome quantity per cell under normoxic versus hypoxic states based on panel (d). (f) Immunoblot detection of migrasome-enriched proteins (PIGK, CPQ, EOGT) and conventional exosome proteins (CD9, TSG101, CD63) to verify the purity of purified migrasomes. * $p < 0.05$, ** $p < 0.01$, *** $p < 0.001$

To determine which cellular populations within tumors account for changes in migrasome output, scRNA-seq datasets from GSE234804 were analyzed to estimate migrasome-forming potential across various lineages. Scoring for migrasome activity indicated that endothelial populations had the highest baseline values, yet these dropped substantially in liver metastatic sites relative to primary tumors, which conflicted with electron microscopy evidence of greater migrasome density in metastases. Endothelial contributions were therefore ruled out. In contrast, both malignant cells and myeloid populations showed pronounced increases in migrasome scores, implicating these as primary sources for migrasomes linked to CRC hepatic spread. To pinpoint specific origins of migrasomes in CRC specimens, attention was directed to three populations—malignant cells, endothelium, and macrophages of myeloid origin—that displayed distinct migrasome scores in the GSE234804 data. Immunofluorescence on patient samples evaluated the overlap between the migrasome indicator TSPAN4 and lineage-specific markers for these groups. Results revealed strong overlap of TSPAN4 mainly with the CRC marker COX-2, where COX-2 levels far exceeded those in other lineages**.** Furthermore, TSPAN4 also overlapped with the macrophage marker CD163, but was rarely seen in endothelial compartments**.** Collectively, these data point to CRC cells as the dominant producers of migrasomes in the tumor milieu.

To substantiate the ability of CRC cells to release migrasomes, primary isolates from patient tumors were cultured and stained with WGA-488. Observations confirmed extensive filopodia bearing numerous WGA-488-positive vesicles **(Figure 1c)**, proving that patient-derived CRC cells actively generate migrasomes. In vitro validation was followed using established CRC lines. Clear retraction fibers and attached migrasomes highlighted by WGA-488 appeared in CT26, HCT116, and MC38 cultures **(Figure 1d)**. Lentiviral delivery of TSPAN4-GFP in P53R cells provided additional evidence of migrasome presence **(Figure 1d)**. Given that low oxygen tension characterizes solid malignancies and drives metastatic progression [25, 26], migrasome production was examined in hypoxic settings. Low-oxygen exposure substantially raised migrasome counts relative to standard conditions **(Figure 1e),** demonstrating that hypoxia stimulates migrasome biogenesis in CRC lines. Immunoblotting of isolates from P53R cells confirmed enrichment of migrasome indicators EOGT, CPQ, and PIGK, with absence of exosome indicators CD9, TSG101, and CD63 **(Figure 1f)**, verifying authentic migrasome purification.

Role of hypoxic migrasomes in enhancing CRC hepatic metastasis

How do migrasomes released by CRC cells in low-oxygen settings affect the tumor ecosystem and metastatic behavior? To explore this, healthy C57BL/6J mice received migrasome injections **(Figure 2a).** Biodistribution tracking with DIR dye revealed hepatic accumulation of administered migrasomes **(Figure 2b)**. A hepatic metastasis model was then created by intrasplenic delivery of tumor cells, combined with intravenous supply of migrasomes generated from MC38 cultures under either normoxic or hypoxic states **(Figure 2c).** MC38 was chosen for ongoing experiments due to its consistent performance in splenic liver metastasis models, unlike CT26. Longitudinal bioluminescence and signal quantification highlighted greater liver tumor load in recipients of hypoxic migrasomes **(Figures 2d and 2e).** Direct inspection of excised livers confirmed that hypoxic-derived migrasomes strongly accelerated CRC seeding in the liver compared to normoxic counterparts **(Figure 2f)**. Taken together, these observations establish that migrasomes produced under hypoxia by CRC cells drive hepatic metastatic dissemination.

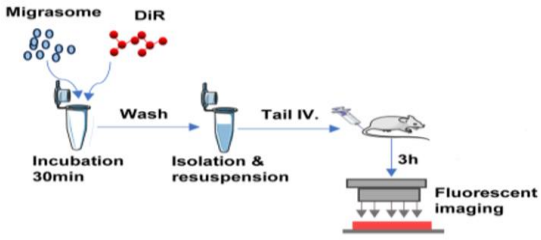

a)

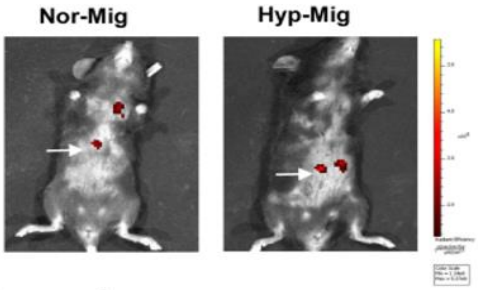

b)

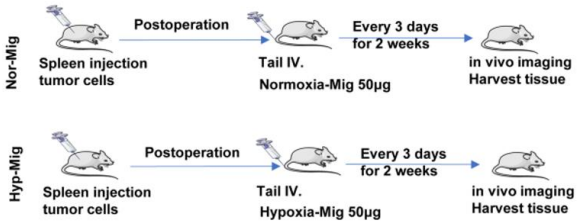

c)

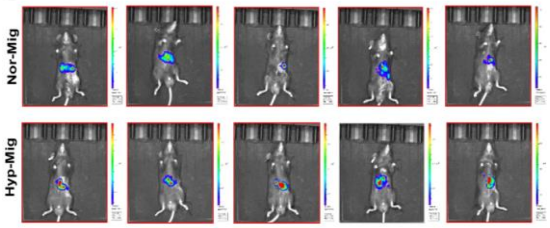

d)

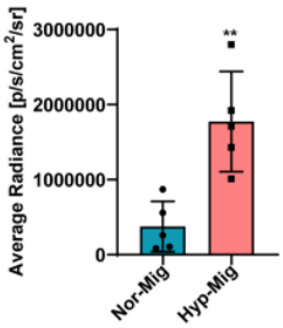

e)

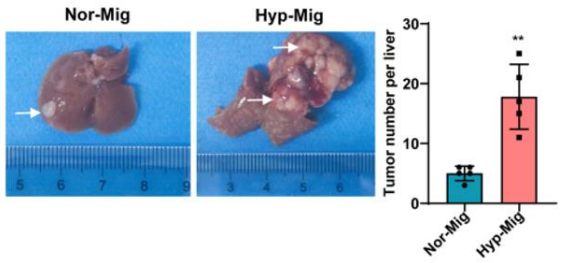

f)

Figure 2. Hypoxic migrasomes enhance colorectal cancer (CRC) hepatic metastasis in living organisms. (a) Outline of the protocol for staining normoxic and hypoxic migrasomes from CRC sources with DiR fluorescent dye, followed by injection into healthy C57BL/6J mice to track tissue distribution in vivo. (b) Typical whole-body fluorescence scans of mice post-injection with DiR-marked normoxic (Nor-Mig) or hypoxic (Hyp-Mig) migrasomes derived from CRC cells. (c) Experimental schedule for inducing CRC liver metastasis via intrasplenic MC38 cell delivery, combined with tail-vein administration of migrasomes produced under normoxic or hypoxic conditions. (d) Longitudinal bioluminescence scans depicting hepatic metastatic lesions, accompanied by signal intensity measurements (e). (f) Photographs of harvested livers displaying metastatic foci (indicated by white arrows) along with counts of surface-visible nodules per organ. n = 5, ** $p < 0.01$

Single-cell RNA sequencing analysis of CRC liver metastases after exposure to normoxic or hypoxic migrasomes

To examine the cellular makeup and gene expression shifts in CRC hepatic metastases influenced by migrasomes from normoxic or hypoxic CRC cultures, single-cell transcriptomic profiling was conducted on tumor samples from the intrasplenic metastasis model. A modest inverse relationship emerged between mitochondrial transcript proportion and total RNA counts ($r = -0.25$), whereas gene detection strongly correlated positively with RNA counts ($r = 0.96$), confirming reliable sequencing depth**.** Dimension reduction via UMAP and clustering revealed 17 separate populations across datasets**.** Annotation assigned these to six broad categories: epithelial, endothelial, fibroblast, myeloid, T lymphocyte, and minor hepatocyte components **(Figure 3a).** The five most characteristic genes per category are shown in dot format**,** highlighting

distinct expression patterns. Proportional breakdown indicated dominance by epithelial cells, then myeloid cells and fibroblasts **(Figure 3b).** Comparison across treatment conditions uncovered 173 genes elevated and 142 reduced in the hypoxic migrasome cohort versus normoxic controls **(Figure 3c).** Leading upregulated genes in the hypoxic cohort—CSN3, CD55, AQP5, SLIT2, and AR—are featured in expression plots **(Figure 3d),** underscoring treatment-specific transcriptional effects. Functional enrichment of differentially expressed genes pointed to strong involvement in "regulation of epithelial cell proliferation" among biological processes **(Figure 3e),** implying heightened growth signals in the metastatic niche. Pathway mapping via KEGG similarly highlighted activation of cancer-promoting routes, notably PI3K-AKT, MAPK, and JAK-STAT cascades **(Figure 3f)**, suggesting that hypoxic migrasomes drive metastatic advancement by engaging several pro-growth and survival networks. Overall, these data indicate that migrasomes generated under low oxygen modify cell populations in CRC liver metastases and trigger oncogenic pathway engagement.

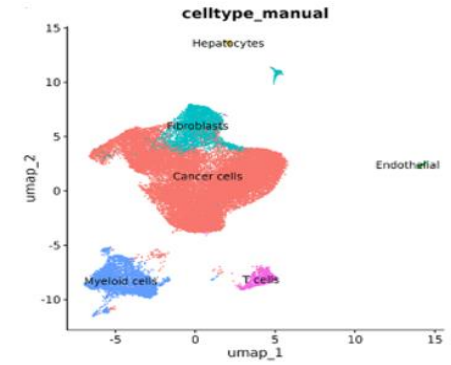

a)

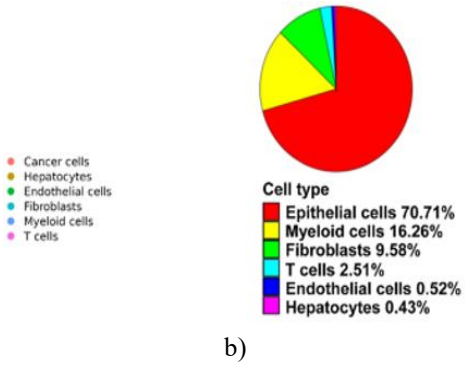

b)

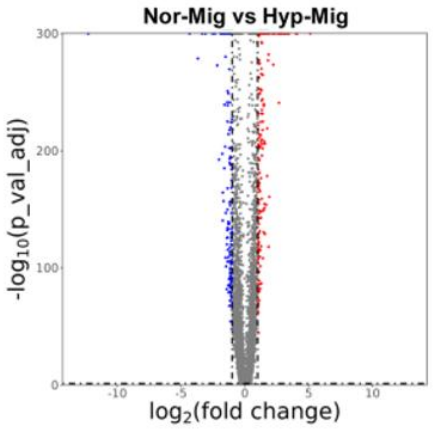

c)

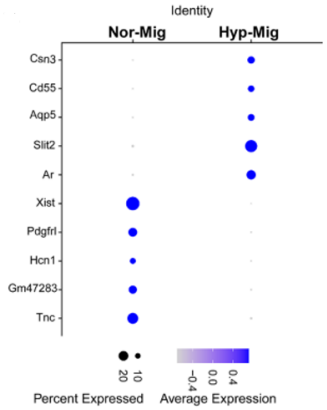

d)

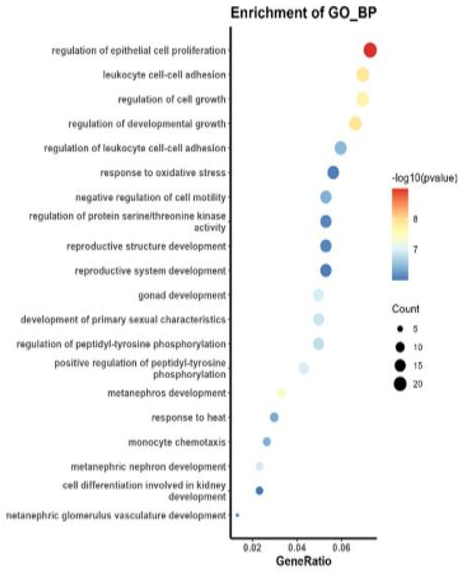

e)

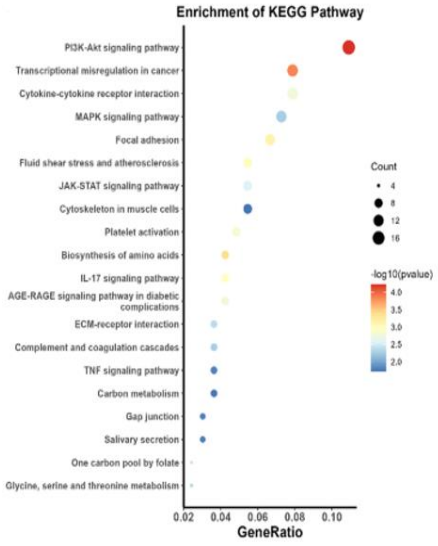

f)

Figure 3. Single-cell gene expression landscape in CRC liver metastases after normoxic or hypoxic migrasome administration. Hepatic metastasis was induced in mice using MC38 cells, followed by treatment with normoxic (Nor-Mig) or hypoxic (Hyp-Mig) migrasomes. Tumor samples from both arms underwent scRNA-seq. (a) Classification of cells in metastatic tissues into six populations: epithelial, endothelial, fibroblast, myeloid, T cell, and hepatocyte. (b) Proportional representation of cell types via a pie chart, dominated by epithelial cells, with myeloid cells and fibroblasts next in abundance. (c) Differential expression visualized as a volcano plot comparing hypoxic versus normoxic conditions; red indicates upregulation and blue downregulation in the hypoxic arm. (d) Dot plot displaying expression levels of the five most prominent differentially regulated genes across groups. (e–f) Enrichment analyses of differentially expressed genes in hypoxic versus normoxic migrasome-exposed metastatic livers. (e) Gene Ontology assessment identifies key biological processes, prominently the regulation of epithelial cell proliferation. (f) KEGG analysis reveals pathway overrepresentation in PI3K-AKT, MAPK, and JAK-STAT signaling.

Hypoxic migrasomes from colorectal cancer cells drive proliferation of Tmem45a⁺ fibroblasts displaying myofibroblast characteristics

Fibroblasts play a pivotal role in metastatic progression by facilitating matrix reorganization, immune regulation, and creation of a metastasis-supportive niche [27]. To explore fibroblast diversity and their contributions in CRC hepatic metastases, subclustering was applied to this lineage. UMAP visualization revealed five separate fibroblast populations **(Figure 4a)**. A cluster-enriched expression profile indicated that the Kif20a⁺ group featured elevated levels of Kif20a, Cenpa, Cenpf, Cdc20, and Ccnb2, while the Tmem45a⁺ group showed strong signals for Tmem45a, Sulf1, Cxcl12, Cdh11, and Bmp5 **(Figure 4b)**. Proportional assessment demonstrated a substantial rise in Tmem45a⁺ fibroblasts within the hypoxic migrasome cohort, accompanied by reductions in the remaining four subtypes **(Figure 4c),** implying selective stimulation of this particular subset by low-oxygen-derived migrasomes. Intercellular interaction mapping via ligand-receptor strength in a chord diagram highlighted predominant PDGF-mediated contacts between fibroblasts and both malignant epithelial cells and macrophages **(Figure 4d).** Pathway scoring through GSVA identified notable upregulation of "adipogenesis" and "complement signaling pathway" specifically in Tmem45a⁺ cells **(Figure 4e)**. Evaluation of the myofibroblast indicator α-SMA (Acta2) disclosed markedly higher levels in the Tmem45a⁺ population relative to others **(Figure 4f)**, pointing to an activated, tumor-favoring myofibroblast state. Trajectory inference reinforced this by positioning Tmem45a⁺ cells chiefly at the terminal branch of fibroblast development **(Figures 4g and 4h)**, consistent with an advanced differentiation stage. Additionally, this subset uniquely displayed robust signals for myofibroblast-associated transcripts COL15A1 and Grem1 **(Figure 4i)**. Together, these observations support a key function for Tmem45a⁺ fibroblasts in reshaping the metastatic ecosystem via myofibroblast-like behavior to advance CRC liver colonization.

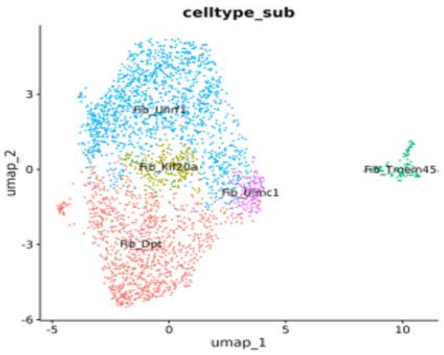

a)

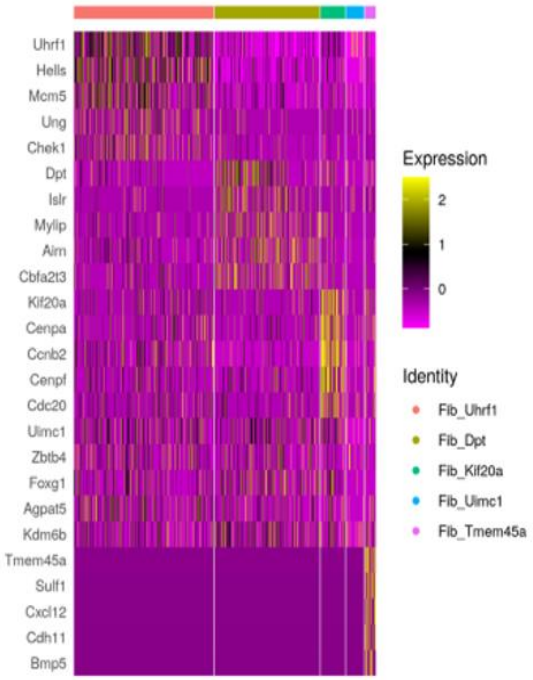
Uhrf1
Hells
Mcm5
Ung
Chek1
Dpt
Islr
Mylip
Aim
Cbfa2t3
Kif20a
Cenpa
Ccnb2
Cenpf
Cdc20
Ulmc1
Zbtb4
Foxg1
Agpat5
Kdm6b
Tmem45a
Sulf1
Cxcl12
Cdh11
Bmp5
Expression
2
1
0
Identity
Fib_Uhrf1
Fib_Dpt
Fib_Kif20a
Fib_Ulmc1
Fib_Tmem45a

b)

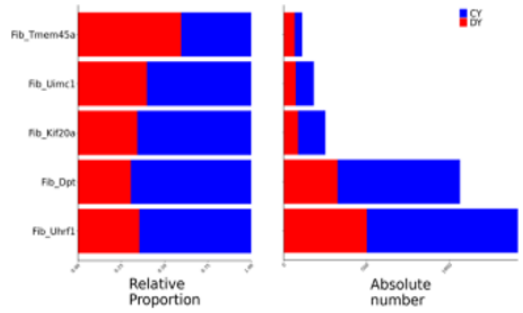
Fib_Tmem45a
Fib_Ulmc1
Fib_Kif20a
Fib_Dpt
Fib_Uhrf1
CY
Dr
Relative Proportion
Absolute number

c)

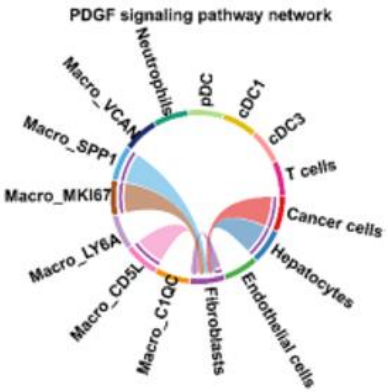
PDGF signaling pathway network
Neutrophils
pDC
cDC1
cDC3
T cells
Cancer cells
Hepatocytes
Endothelial cells
Fibroblasts
Macro_C1QC
Macro_CD5L
Macro_LY6A
Macro_MKI67
Macro_SPP1
Macro_VCAN

d)

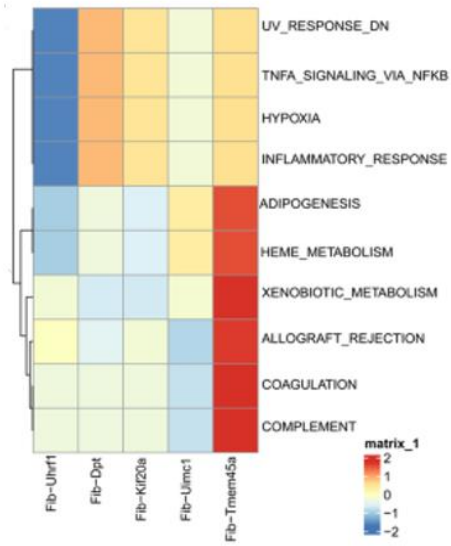
UV_RESPONSE_DN
TNFA_SIGNALING_VIA_NFKB
HYPOXIA
INFLAMMATORY_RESPONSE
ADIPOGENESIS
HEME_METABOLISM
XENOBIOTIC_METABOLISM
ALLOGRAFT_REJECTION
COAGULATION
COMPLEMENT
Fib-Uhrf1
Fib-Dpt
Fib-Kif20a
Fib-Ulmc1
Fib-Tmem45a
matrix_1
2
1
0
−1
−2

e)

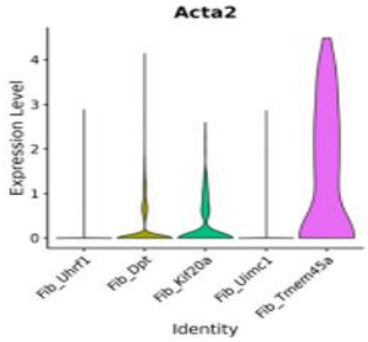
Acta2
Expression Level
4
3
2
1
0
Fib_Uhrf1
Fib_Dpt
Fib_Kif20a
Fib_Ulmc1
Fib_Tmem45a
Identity

f)

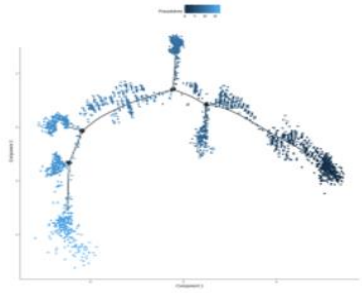

g)

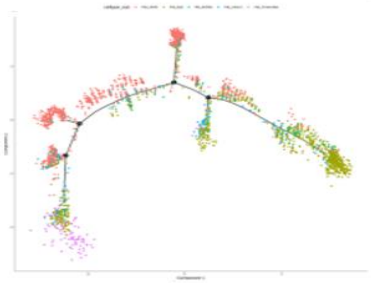

h)

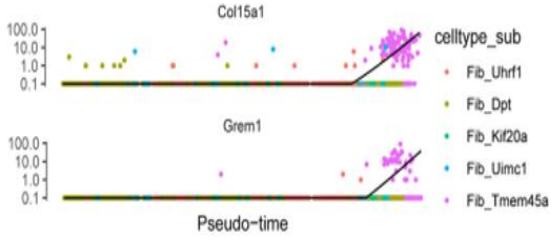

i)

Figure 4. Low-oxygen CRC migrasomes stimulate growth of Tmem45a$^+$ fibroblasts exhibiting myofibroblast traits. (a) UMAP representation of five fibroblast subclusters derived from detailed analysis. (b) Expression heatmap of key signature genes across clusters, with the Kif20a$^+$ group enriched in proliferation-related markers (Kif20a, Cenpa, Cenpf, Cdc20, Ccnb2) and the Tmem45a$^+$ group in Tmem45a, Sulf1, Cxcl12, Cdh11, and Bmp5. (c) Comparative bar graph of subset proportions between normoxic and hypoxic migrasome conditions, showing marked expansion of Tmem45a$^+$ cells in the hypoxic arm. CY: normoxic migrasomes (Nor-Mig); DY: hypoxic migrasomes (Hyp-Mig). (d) Chord diagram depicting inferred communication patterns, emphasizing PDGF pathway links connecting fibroblasts to epithelial tumor cells and macrophages. (e) GSVA results highlighting complement pathway activation in Tmem45a$^+$ fibroblasts. (f) Violin distribution illustrating higher Acta2 (α-SMA) levels in Tmem45a$^+$ cells, indicative of myofibroblast activation. (g–h) Developmental trajectory mapping placing Tmem45a$^+$ fibroblasts mainly at the endpoint of differentiation. (g) Pseudotime path with gradient coloring from early (dark) to late (light) states. (h) Subtype allocation along the inferred trajectory. (i) Expression maps revealing prominent COL15A1 and Grem1 signals restricted to Tmem45a$^+$ fibroblasts, linked to myofibroblast conversion.

Single-cell profiling uncovers a distinct CD5L$^+$ macrophage population with enhanced efferocytosis triggered by hypoxic CRC migrasomes

Since myeloid lineage forms the second largest component in the metastatic milieu following malignant epithelial cells **(Figure 3b)**, deeper examination targeted myeloid heterogeneity. Reclustering yielded 10 discrete myeloid groups **(Figure 5a)**. Signature gene patterns per group are depicted in the heatmap **(Figure 5b).** The CD5L$^+$ macrophage group displayed the greatest expansion under hypoxic migrasome exposure, achieving roughly eightfold higher representation than in normoxic controls **(Figures 5c)**, prompting focused investigation of this population. Pathway enrichment via GSVA detected strong signals for "coagulation" and "complement signaling pathway" in CD5L$^+$ macrophages **(Figure 5d)**. Interaction inference through chord visualization suggested GDF pathway-driven connections from this subset to fibroblasts, T lymphocytes, and additional immune elements **(Figure 5e)**. This group also showed selective IGF1 elevation, implicating IGF-mediated crosstalk with tumor cells **(Figures 5f and 5g).** Exclusive high CD5L expression confirmed the subset identity **(Figure 5h).** Interestingly, the migrasome indicator TSPAN4 appeared in multiple macrophage groups **(Figures 6a)**. Additional migrasome-associated transcripts NDST1 and CD81 were similarly noted in CD5L$^+$ cells**.** Functional scoring positioned CD5L$^+$ macrophages as having the peak efferocytosis activity across all 10 myeloid categories **(Figure 6b)**. Supporting this, dedicated efferocytosis genes, including CD300LB, MERTK, and CD300LD, reached the highest levels in this population **(Figures 6c)**, underscoring their specialized clearance role.

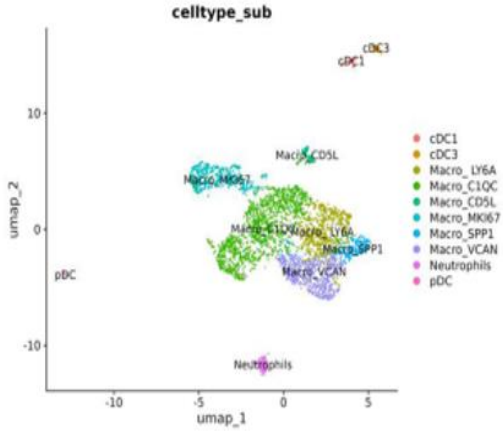

a)

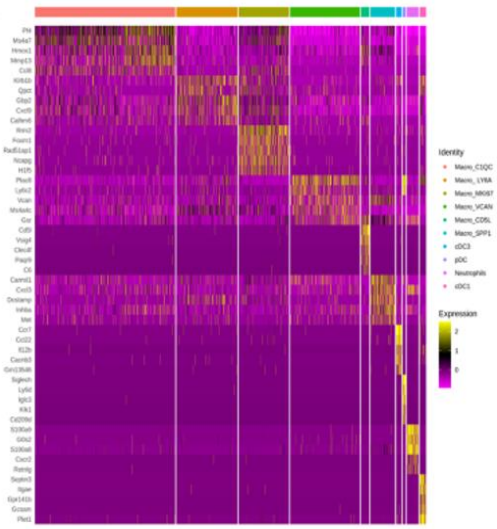

b)

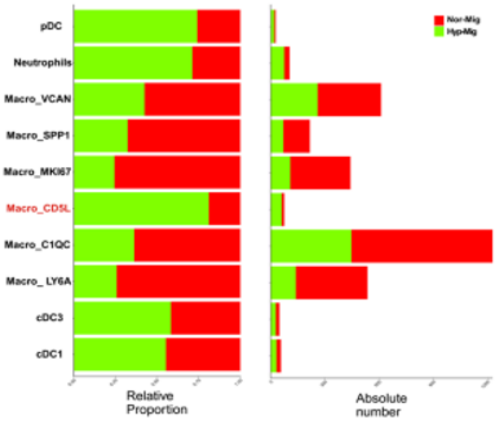

c)

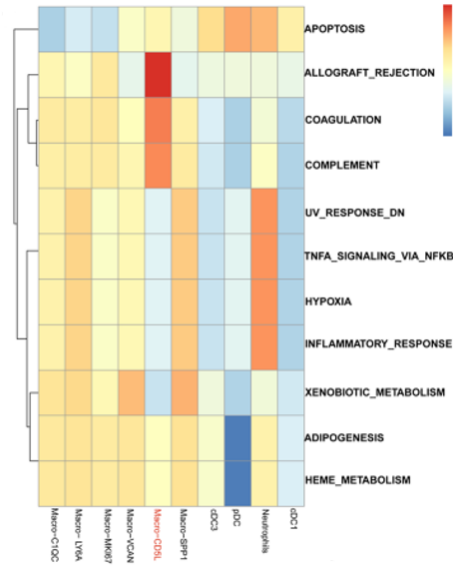

d)

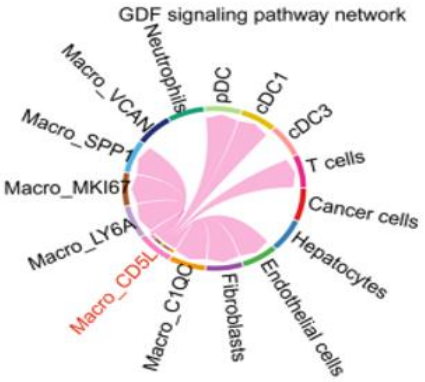

e)

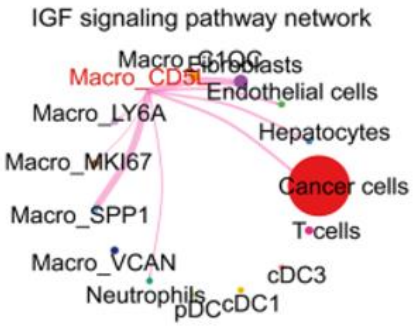

f)

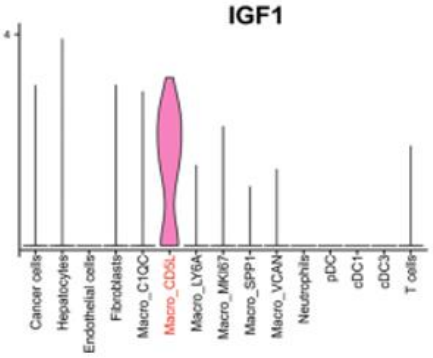

g)

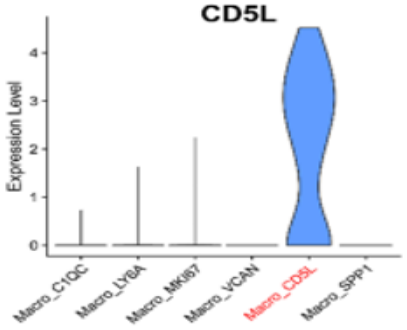

h)

Figure 5. Analysis of myeloid populations and recognition of CD5L^{+} macrophages as cells

responsive to migrasomes. (a) UMAP display illustrating the subdivision of myeloid lineage into 10 separate groups. (b) Expression heatmap of key signature genes defining each myeloid group. (c) Comparative bar graph of subpopulation proportions between normoxic and hypoxic migrasome conditions, highlighting an approximately 8-fold rise in CD5L⁺ macrophages under hypoxic exposure. (d) GSVA results demonstrating pronounced complement pathway engagement in CD5L⁺ macrophages. (e) Chord visualization of predicted intercellular links, emphasizing GDF-mediated contacts from CD5L⁺ macrophages to fibroblasts, T lymphocytes, and additional immune components. (f) Depiction of IGF pathway-driven interactions facilitating communication between CD5L⁺ macrophages and malignant epithelial cells. (g) Within the IGF network, CD5L⁺ macrophages selectively overexpress IGF1. (h) Across the six macrophage categories, CD5L⁺ cells uniquely show elevated CD5L levels.

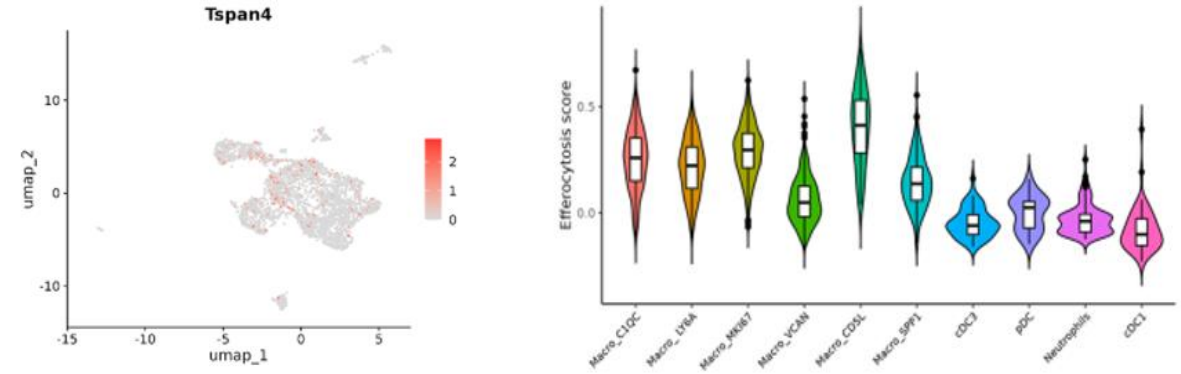

a) b)

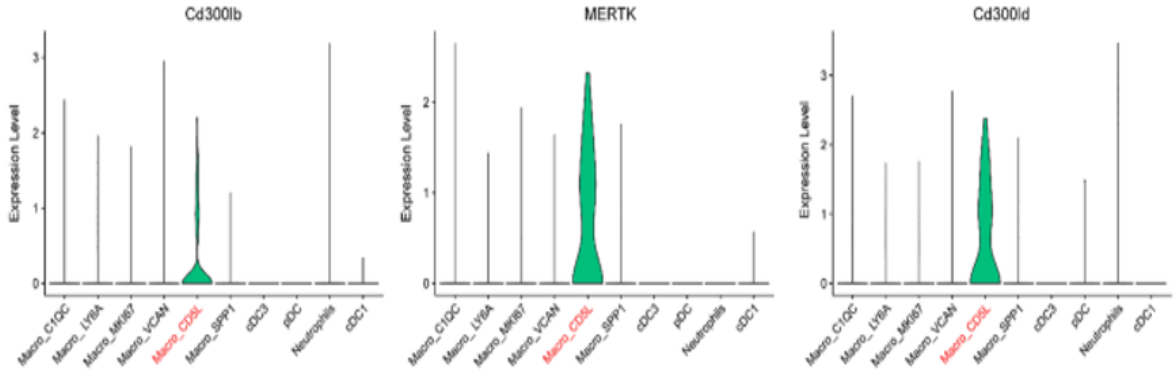

c)

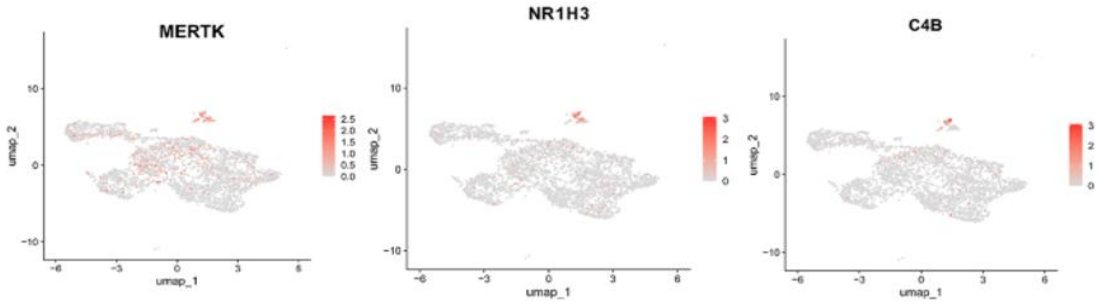

d)

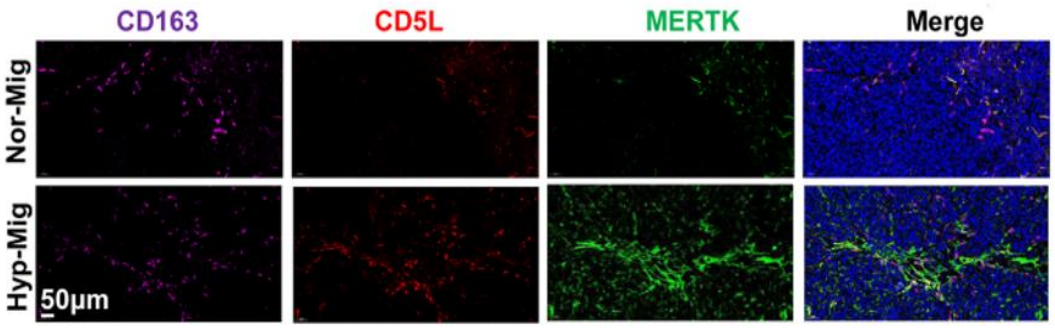

e)

Figure 6. Evaluation of engulfment capability and immunofluorescence confirmation of CD5L⁺ macrophages in CRC hepatic metastases after migrasome administration. (a) UMAP representation of migrasome indicator TSPAN4 distribution across myeloid groups. (b) Boxplot comparing efferocytosis activity scores among the 10 myeloid categories. (c) Violin distributions of efferocytosis-associated genes CD300B, MERTK, and CD300D in the 10 myeloid populations. (d) UMAP views highlighting the expression of three clearance-related markers predominantly enriched in CD5L⁺ macrophages. (e) Immunofluorescence on tumor samples from MC38-bearing mice revealing overlap of CD163, CD5L, and clearance indicator MERTK in both arms, with stronger MERTK signals in the hypoxic cohort, implying greater migrasome influence on CD5L⁺ macrophages.

To explore gene expression distinctions between CD5L⁺ macrophages and remaining macrophage groups (combined as other), differential analysis was conducted. Relative to the other category, CD5L⁺ cells displayed 690 upregulated and 492 downregulated transcripts. Leading upregulated genes included CLEC4F, PAQR9, C6, CD5L, and VSIG4. A substantial set of clearance-linked genes reached high levels in CD5L⁺ cells, such as MERTK, NR1H, C4B, CD36, ARHGAP25, and PLA2G15 **(Figures 6d).** Biological process enrichment via GO prominently featured "phagocytosis", while KEGG highlighted "efferocytosis" pathway activation**.** These patterns suggest a specialized transcriptomic signature conferring superior clearance ability to CD5L⁺ macrophages.

Overall, the data prompted the proposal that CD5L⁺ macrophages act as primary targets for migrasomes released by hypoxic CRC cells, and that hypoxic migrasome exposure substantially boosts their clearance performance. Supporting this, immunofluorescence on metastatic tissues from mice treated with either hypoxic or normoxic migrasomes employed CD163 and CD5L to mark the subset, paired with MERTK as a clearance indicator. Strong triple overlap of CD163, CD5L, and MERTK appeared in samples from both conditions **(Figure 6e).** Strikingly, CD5L and MERTK signals intensified in the hypoxic arm **(Figure 6e)**, indicating activation of clearance function in CD5L⁺ macrophages by low-oxygen migrasomes. In summary, single-cell profiling has uncovered a novel CD5L-expressing macrophage population that demonstrates clearance activity triggered by hypoxic migrasomes in colorectal cancer.

Low-oxygen migrasomes from CRC sources stimulate maturation and clearance function in CD5L⁺ macrophages

Building on observations in **Figure 6** that point to CD5L⁺ macrophages with elevated clearance scores as likely migrasome recipients, further experiments tested if hypoxic CRC migrasomes drive development and engulfment activity in this group. Murine bone marrow precursors were harvested and matured into macrophages ex vivo, then exposed to MC38-sourced migrasomes for 24 h. Flow cytometric quantification showed a clear rise in CD5L⁺ fraction after hypoxic migrasome treatment versus normoxic **(Figure 7a),** underscoring induction of this subset. To assess functional gain, CD5L⁺ cells were isolated via sorting **(Figure 7b)** and incubated with PI-marked dying MC38 cells. F4/80 immunostaining revealed substantially greater internalization of red-labeled apoptotic targets by CD5L⁺ macrophages pretreated with hypoxic migrasomes **(Figures 7c-7d).** In combination, these results demonstrate that hypoxic CRC migrasomes foster both the emergence of CD5L⁺

macrophages and their enhanced engulfment of apoptotic cells.

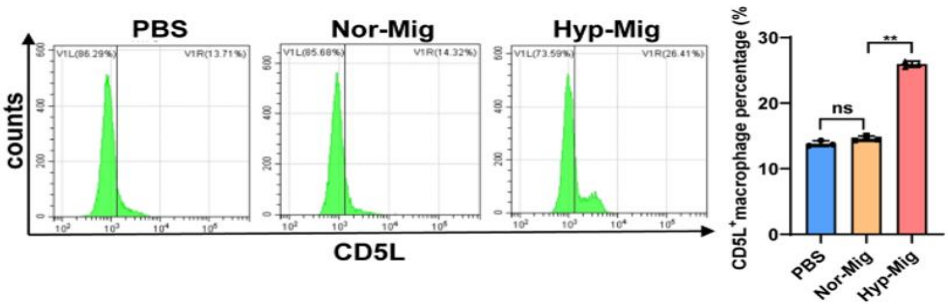

a)

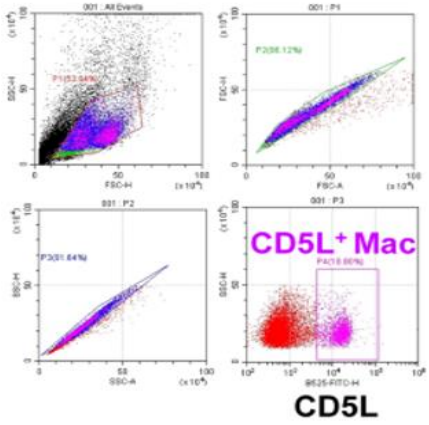

b)

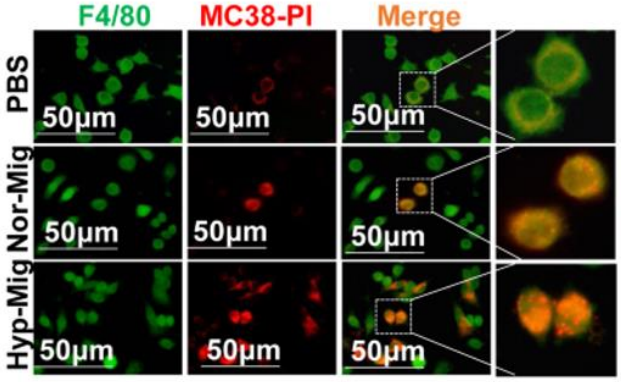

c)

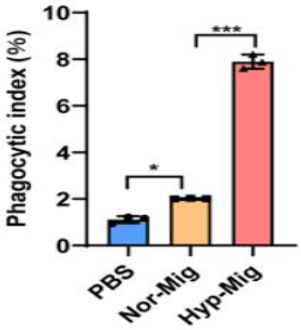

d)

Figure 7. Low-oxygen migrasomes from colorectal cancer cells stimulate maturation and clearance activity in CD5L$^+$ macrophages. (a) Flow cytometric assessment of CD5L$^+$ macrophage frequency following 24 h exposure to migrasomes isolated from normoxic or hypoxic CRC sources. (b) Sorting strategy via flow cytometry for purifying CD5L$^+$ macrophages. (c) Immunofluorescence evaluation of clearance function in CD5L$^+$ macrophages. Isolated CD5L$^+$ cells were incubated with PI-stained dying MC38 cells post-migrasome exposure. F4/80 (green) identifies macrophages; PI (red) labels dying tumor cells. Typical micrographs highlight greater engulfment of dying cells by CD5L$^+$ macrophages pretreated with hypoxic migrasomes. Scale bar: 50 μm. (d) Quantification of clearance capacity in CD5L$^+$ macrophages using phagocytic index. ns $p > 0.05$, ** $p < 0.01$

Migrasomes from CRC cells deliver NRP2 to macrophages

To uncover how hypoxic CRC migrasomes drive $CD5L^{+}$ macrophage development and clearance, proteomic profiles of CRC migrasomes were examined from the ProteomeXchange repository. In total, 601 proteins showed strong enrichment in migrasomes **(Figure 8a).** Overlap with clearance-related proteins yielded two candidates—Neuropilin-2 (NRP2) and Calreticulin (CALR)—present at higher levels in migrasomes **(Figure 8a).** Immunoblotting confirmed marked elevation of both CALR and NRP2 in hypoxic-derived migrasomes relative to normoxic ones at equivalent loading **(Figure 8b)**. This pattern held steady using either GAPDH or the migrasome indicator CPQ for loading control, affirming reliable quantification. Variation coefficients were similar across both normalization approaches, ruling out bias from GAPDH distribution. Strikingly, only NRP2—not CALR—rose substantially in macrophages after hypoxic migrasome exposure **(Figure 8c)**, implicating NRP2 in macrophage functional shifts induced by hypoxic migrasomes. Patient CRC samples similarly displayed higher NRP2 in malignant tissue versus nearby normal areas **(Figure 8d).** Consistent with this, TCGA-COAD data indicated poorer overall survival in cases with elevated NRP2 **(Figure 5a).**

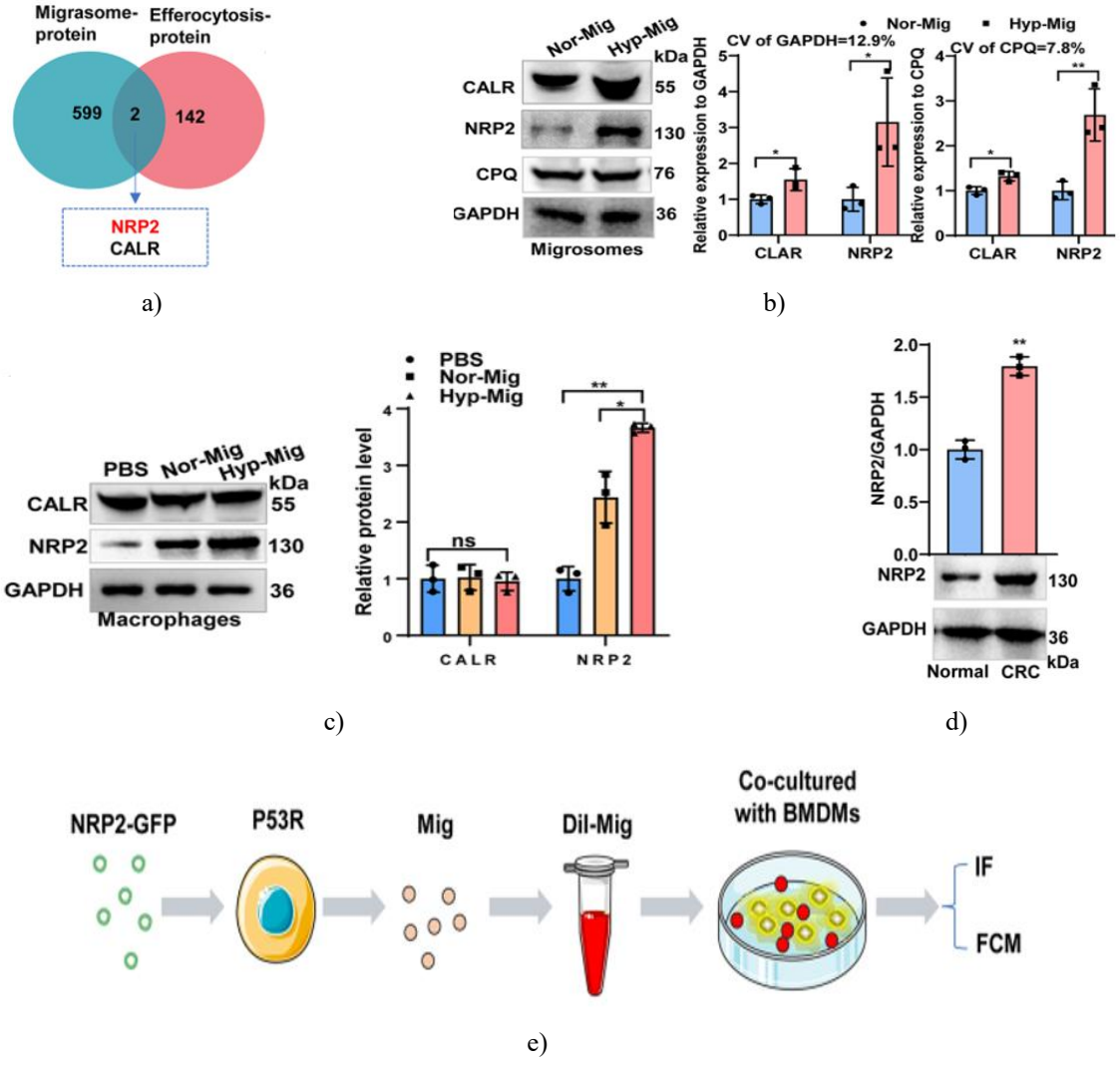

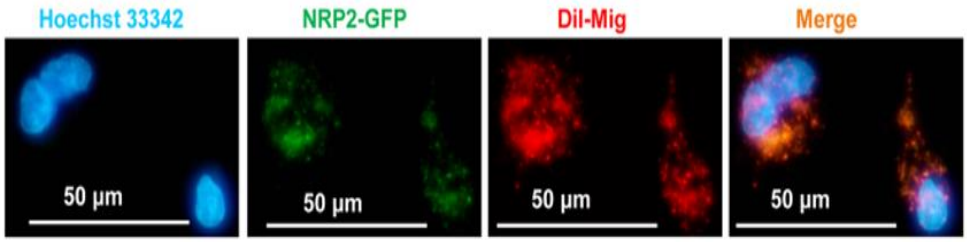

f)

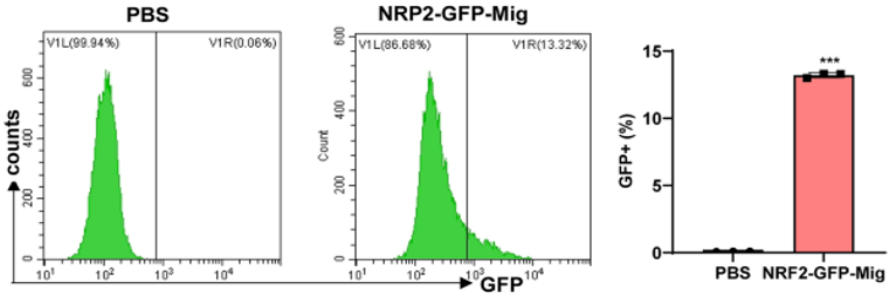

g)

Figure 8. Migrasomes originating from CRC transfer NRP2 into macrophages. (a) Venn representation of overlap between migrasome-enriched proteome and clearance-linked proteins, pinpointing NRP2 and CALR. (b) Immunoblot detection of NRP2 and CALR in migrasomes from normoxic versus hypoxic CRC cultures at matched loading. Normalization employed GAPDH and migrasome-specific CPQ, with densitometry showing consistent trends and comparable variation coefficients (CV). (c) Immunoblot assessment of NRP2 and CALR levels in macrophages post-exposure to normoxic or hypoxic CRC migrasomes. (d) Immunoblot of NRP2 in paired clinical CRC tumor and adjacent samples. (e) Experimental outline for monitoring uptake of NRP2-GFP-tagged migrasomes by macrophages. (f) Typical immunofluorescence micrographs demonstrating overlap of NRP2-GFP (green) and DiI-stained migrasomes (red) inside macrophages. Hoechst 33,342 counters nuclear DNA (blue). Scale bar: 50 µm. (g) Flow cytometric detection of GFP signal in macrophages after incubation with NRP2-GFP-carrying migrasomes, confirming internalization. ns $p > 0.05$, * $p < 0.05$, ** $p < 0.01$, *** $p < 0.001$

To confirm migrasome-mediated delivery of NRP2 to macrophages, hypoxic MC38 cells were engineered to express NRP2-GFP, isolated migrasomes were marked with DiI, and then added to bone marrow-derived macrophages **(Figure 8e)**. Fluorescence imaging showed clear merger of NRP2-GFP (green) and DiI (red) signals within macrophages, evidencing migrasome engulfment carrying NRP2 **(Figure 8f)**. Additionally, flow analysis detected a clear increase in GFP-expressing macrophages following NRP2-migrasome treatment over PBS controls **(Figure 8g).** These observations indicate that hypoxic CRC migrasomes actively shuttle NRP2 into macrophages, likely underlying subsequent cellular responses.

Migrasomes from colorectal cancer cells deliver NRP2 to macrophages, driving clearance-linked functional shifts

To confirm if migrasomes from CRC sources control $CD5L^+$ macrophage maturation and clearance activity through NRP2 shuttling, NRP2 expression was suppressed in hypoxic MC38 cultures **(Figures 9a and 9b)**, yielding migrasomes depleted of NRP2. Exposure of bone marrow-derived macrophages to these NRP2-lacking migrasomes led to a clear drop in $CD5L^+$ macrophage frequency relative to treatment with intact migrasomes **(Figure 9c)**. In line with this, engulfment of dying tumor cells by $CD5L^+$ macrophages was notably weakened without migrasome-carried NRP2 **(Figure 9d).** Additionally, both transcript and protein abundance of major clearance receptors—MERTK, TYRO3, OLR1, CD36, AXL, and TIM3—declined in macrophages receiving NRP2-deficient migrasomes, underscoring NRP2's essential contribution to the clearance phenotype **(Figures 9e and 9f)**. Overall, these data establish that low-oxygen migrasomes from CRC

cells stimulate CD5L⁺ macrophage emergence and clearance performance by transporting NRP2.

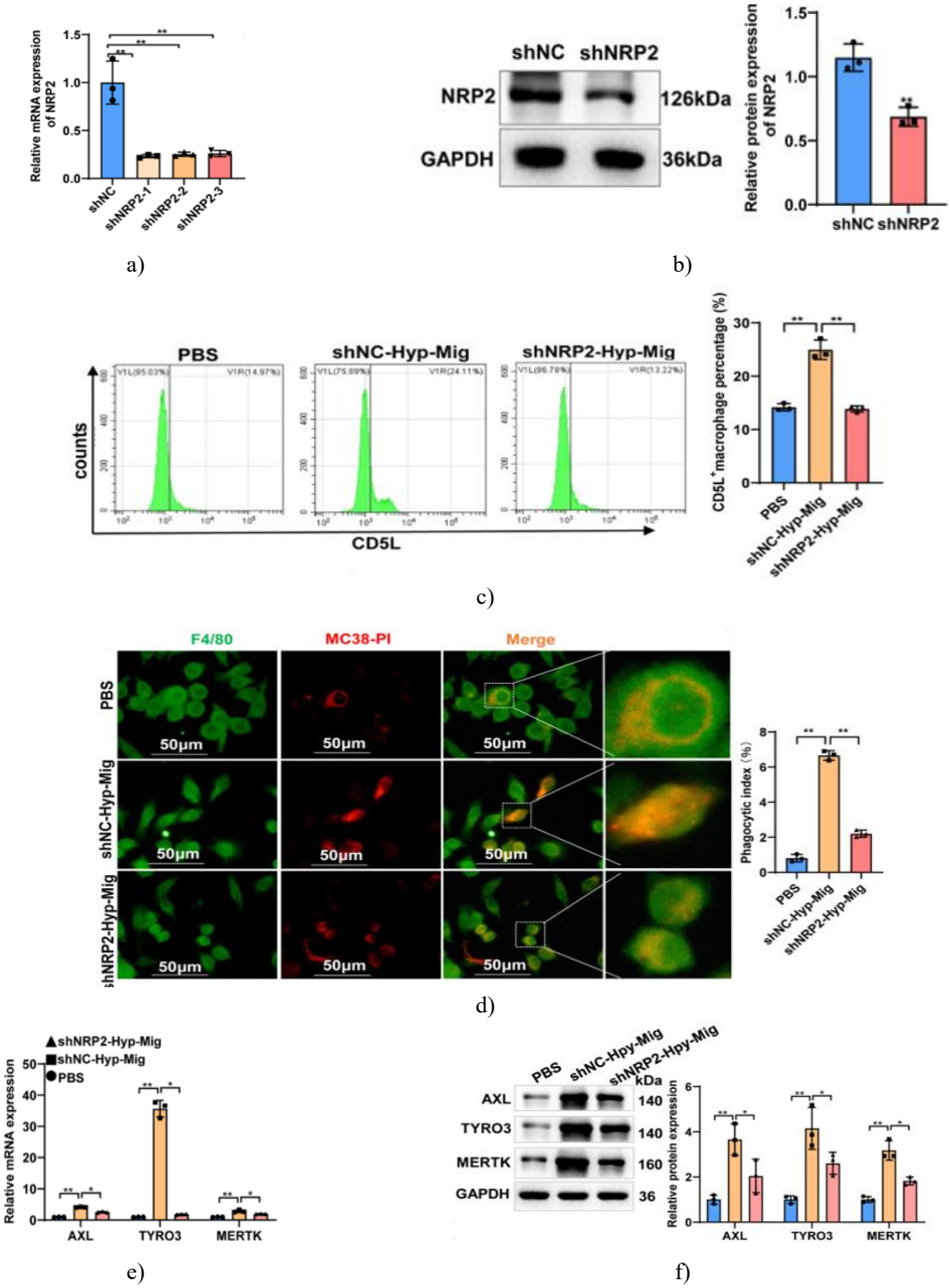

Figure 9. Migrasome-associated NRP2 is essential for CRC-triggered CD5L⁺ macrophage maturation and clearance function. (a) Quantitative RT-PCR verification of effective NRP2 silencing in hypoxic MC38 cells. (b) Immunoblot confirmation of successful NRP2 reduction in hypoxic MC38 cells. (c) Flow cytometric measurement of CD5L⁺ macrophage percentage after exposure to control versus NRP2-depleted hypoxic

migrasomes from MC38 sources. (d) Immunofluorescence evaluation of clearance in CD5L⁺ macrophages treated with control or NRP2-depleted hypoxic migrasomes. F4/80 (green) identifies macrophages; PI (red) marks dying tumor cells. Scale bar: 50 μm. (e) RT-qPCR-based measurement of transcript levels for clearance receptors (MERTK, TYRO3, OLR1, CD36, AXL, and TIM3) in macrophages exposed to control or NRP2-lacking migrasomes. (f) Immunoblot-based assessment of protein levels for the same clearance receptors (MERTK, TYRO3, OLR1, CD36, AXL, and TIM3) under identical conditions. * $p < 0.05$, ** $p < 0.01$

NRP2 engages PROX1 to orchestrate CD5L⁺ macrophage maturation and clearance activity

To clarify how NRP2 governs CD5L⁺ macrophage development and clearance, potential binding partners were forecasted via the STRING resource, yielding 73 candidates**.** Since transcription factors predominantly direct cell identity and may control clearance-associated genes, the 73 interactors were cross-referenced with transcription factors from AnimalTFDB. Overlap analysis identified three shared entries—NR2F2, PROX1, and SOX18**.** GEPIA2 profiling revealed exclusive significant elevation of PROX1 in COAD specimens over normal counterparts among the trio**.** Thus, PROX1 was prioritized as the likely downstream partner of NRP2.

Physical binding between NRP2 and PROX1 was tested by co-immunoprecipitation using anti-NRP2 in macrophages with or without hypoxic migrasome exposure **(Figure 10a).** Immunoblotting confirmed robust PROX1 pull-down by NRP2 across conditions, validating their association. Spatial overlap was further evidenced by immunofluorescence showing close proximity of NRP2 and PROX1 **(Figure 10b)**. To assess if NRP2 influences macrophage behavior via PROX1, concurrent NRP2 elevation and PROX1 suppression were introduced in macrophages. Overexpression and silencing efficiencies were verified by quantitative PCR**.** NRP2 elevation strongly boosted CD5L levels and expanded CD5L⁺ macrophage representation **(Figure 10c)**, while PROX1 reduction produced opposing outcomes; combined manipulation largely neutralized NRP2's impact. Parallel transcript analysis indicated NRP2 elevation raised AXL, MERTK, and TYRO3 mRNA, whereas PROX1 loss lowered them, with dual treatment blunting these shifts **(Figure 10d).** Fluorescence imaging of F4/80-marked macrophages engulfing PI-labeled MC38 remnants showed PROX1 suppression markedly diminished clearance in CD5L⁺ cells and partly countered NRP2's stimulatory role **(Figure 10e).** In summary, these observations indicate that NRP2 advances CD5L⁺ macrophage emergence and clearance capability through PROX1-mediated transcriptional control.

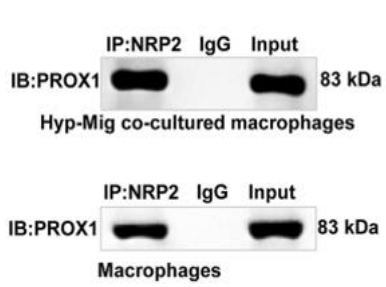

a)

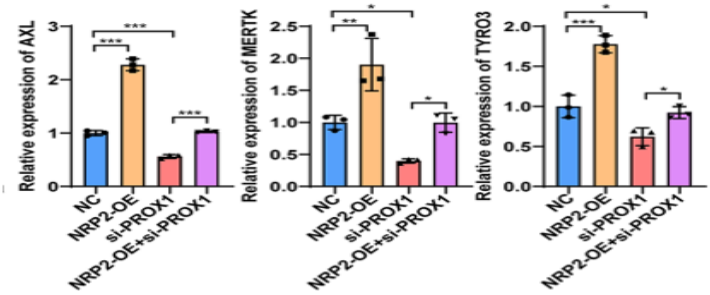

d)

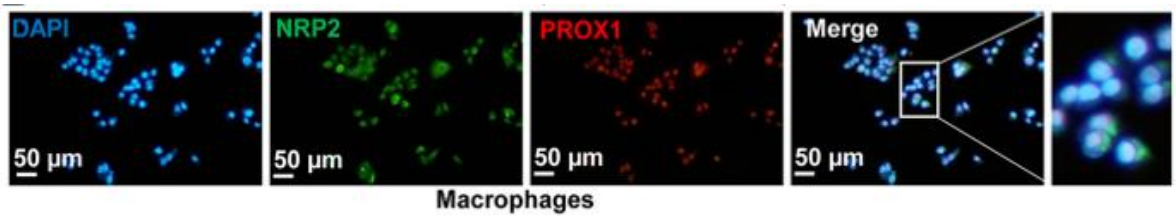

b)

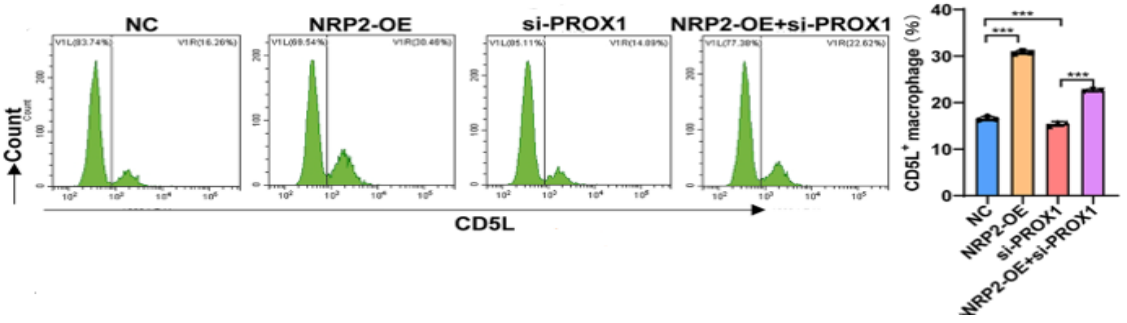

c)

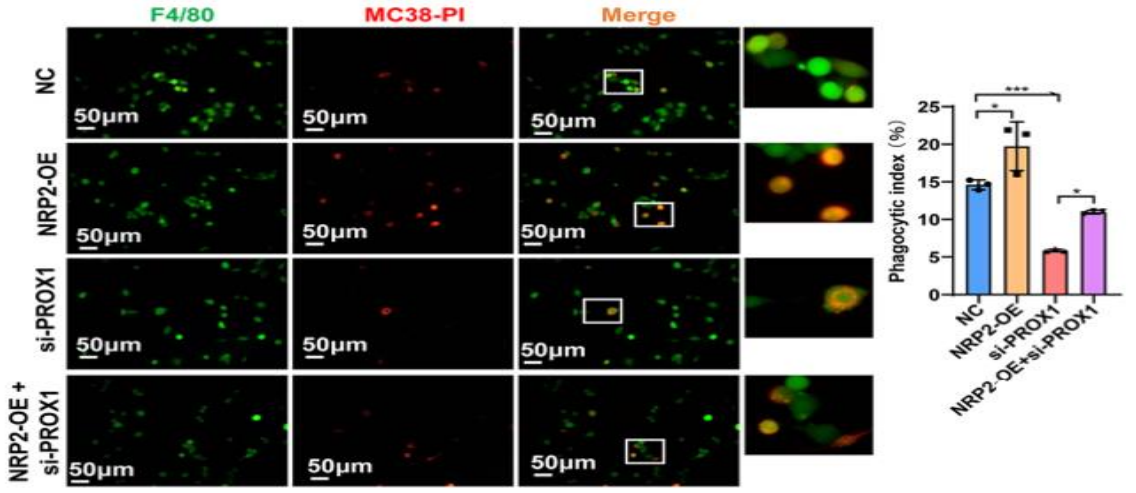

e)

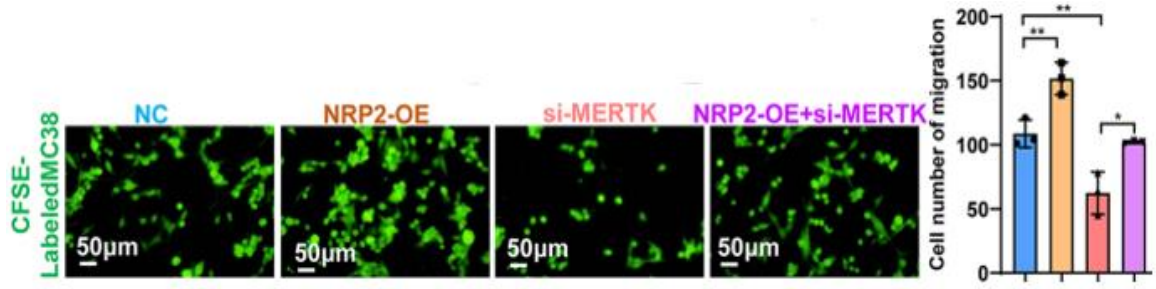

f)

Figure 10. Binding between NRP2 and PROX1 stimulates CD5L⁺ macrophage maturation and boosts clearance performance. (a) Co-immunoprecipitation experiments demonstrating NRP2 association with PROX1 in macrophages exposed to normoxic or hypoxic migrasomes. (b) Immunofluorescence micrographs illustrating the close proximity of NRP2 (green) and PROX1 (red) in macrophages. Nuclear counterstain used DAPI (blue). Scale bar, 50 μm. (c) Flow cytometric evaluation of CD5L⁺ macrophage frequency after NRP2 elevation and/or PROX1 suppression. (d) Quantitative RT-PCR measurement of clearance-associated transcripts (AXL, MERTK, and TYRO3) in macrophages under specified modifications. (e) Immunofluorescence detection of F4/80-positive macrophages (green) internalizing PI-marked dying MC38 fragments (red). PROX1 reduction diminished clearance activity and partly countered NRP2-driven stimulation. Scale bar, 50 μm. (f) Typical fluorescence micrographs and counts from transwell migration experiments. CFSE-stained CRC cells were incubated with macrophages featuring NRP2 elevation, MERTK suppression, or both combined, followed by assessment of CRC transmigration. * $p < 0.05$, ** $p < 0.01$, *** $p < 0.001$

To explore the contribution of macrophage clearance to metastatic advancement, prior reports indicate that MERTK-driven engulfment not only reinforces macrophage immunosuppression but also accelerates tumor spread by fostering a restrictive niche [21]. In colorectal cancer, M2-polarized macrophage clearance has been linked to dampened cytotoxic T cell responses via STING/IFN-I blockade [22], and targeted MERTK inhibition substantially curbs tumor expansion and hepatic seeding [23]. These observations position clearance as a central metastatic facilitator. To test if NRP2 advances CRC metastasis via macrophage clearance, CFSE-marked CRC cells were paired with macrophages either elevated for NRP2 or depleted of MERTK, then migration was monitored in transwell setups. Imaging revealed strong promotion of CRC movement by NRP2-enhanced macrophages, countered by MERTK loss. Dual manipulation partly offset NRP2's migratory boost **(Figures 10f)**, implying that NRP2-expressing macrophages drive CRC mobility at least partially through MERTK-reliant clearance.

Since macrophage-secreted factors critically fuel metastatic dissemination [28], the possibility of additional secretory roles for NRP2-primed $CD5L^+$ macrophages beyond clearance was examined. Annexin V/PS liposomes were applied to disrupt "eat-me" signal binding, thus blocking $CD5L^+$ macrophage clearance, and conditioned media (CM) were harvested from various conditions**.** Exposure of CRC cells to these CMs showed heightened invasion and movement with $CD5L^+$ macrophage CM over controls**.** Blocking clearance attenuated this stimulation. Interestingly, CM from hypoxic migrasome-exposed plus clearance-blocked $CD5L^+$ macrophages partly recovered CRC invasive and migratory capacity. Even after clearance inhibition, hypoxic migrasomes retained migratory promotion, pointing to an independent secretory pathway supporting CRC movement. Supporting this, ELISA detected elevated immunosuppressive factors IL-10, TGF-β, and CCL2 in $CD5L^+$ macrophage CM versus controls. Clearance blockade lowered these secretions, but hypoxic migrasome addition under blockade partly reinstated them. To link hypoxic migrasome effects on cytokine output to NRP2/PROX1 signaling in $CD5L^+$ macrophages, transcript levels of IL-10, TGF-β, and CCL2 were measured in macrophages with NRP2 elevation or PROX1 suppression. NRP2 boost raised these cytokines markedly over controls, while PROX1 loss decreased them**.** Concurrent PROX1 suppression partly neutralized NRP2-driven cytokine increase, indicating that the NRP2/PROX1 pathway also amplifies secretory immunosuppressive actions in $CD5L^+$ macrophages.

Hepatic spread dominates distant metastasis in colorectal cancer and accounts for most CRC deaths. Advances have clarified several drivers of liver colonization—including gut microbiota [29], tumor-associated fibroblasts [14], and immune regulation [30]—yet the influence of hypoxic tumor ecosystems on niche formation remains partially mapped. Specifically, interactions between tumor-released migrasomes and immune populations during metastasis are underexplored. Here, we show that low-oxygen-triggered migrasomes from CRC cells shuttle NRP2 into macrophages, fostering the emergence of a $CD5L^+$ macrophage group with heightened clearance ability via PROX1 engagement **(Figure. 11)**. These results uncover a previously unknown migrasome-based communication route between tumor and immune cells, and propose that disrupting tumor-macrophage crosstalk through migrasome payloads like NRP2 could offer fresh strategies against CRC hepatic metastasis.

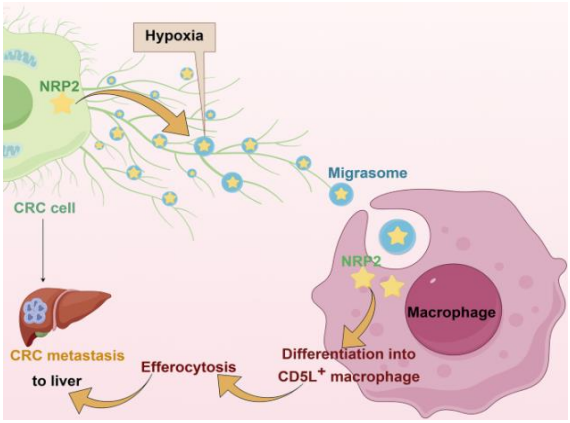

Figure 11. Illustrative overview of the suggested pathway. Diagram encapsulating the central discoveries of this research. Low-oxygen colorectal cancer cells produce migrasomes loaded with NRP2, which are selectively internalized by macrophages within the hepatic metastatic niche. Delivered NRP2 via migrasomes stimulates the emergence of $CD5L^+$ macrophages and amplifies their clearance capability. Such $CD5L^+$ macrophages help establish a metastasis-favoring ecosystem that supports CRC seeding in the liver. Generated using Figdraw (http://www.figdraw.com) with technical assistance (WIRYY15135)

In this work, we reveal that the migrasome–NRP2 pathway from CRC orchestrates macrophage adaptability and drives immune reconfiguration in the hepatic metastatic setting. Since migrasomes were identified only recently, their physiological functions are still largely unexplored, and no earlier reports, to our knowledge, have addressed their participation in CRC liver colonization. However, data from other cancers underscore migrasomes' importance in advancing tumor growth and spread. For example, higher CD151 levels boost migrasome formation, and CD151-carrying migrasomes from liver cancer cells have been found to stimulate invasion and vessel formation [16]. This investigation is the first to show that migrasomes released by CRC cells can alter macrophage subgroups. So far, just two publications have examined migrasome-facilitated interactions in tumor ecosystems. One demonstrated that pancreatic cancer migrasomes contain diverse chemokines, cytokines, and signaling molecules that shift macrophages toward an immune-suppressive M2 state, fueling tumor advancement [31]. Another, applying single-cell and spatial transcriptomics, described TSPAN4-expressing fibroblasts with elevated migrasome production that engage various immune cells, including macrophages, aiding pancreatic cancer spread and immune alteration [32]. These reports align with our observation that CRC migrasomes reshape the liver metastatic milieu by directly modifying macrophage characteristics.

This research pinpoints NRP2 as a vital payload in migrasomes that strengthens maturation and clearance performance in $CD5L^+$ macrophages. NRP2 is part of the neuropilin family of single-pass transmembrane proteins featuring brief cytoplasmic tails [33]. Lacking built-in kinase domains, they depend on partners like VEGF receptors or plexins for signal transduction. NRP2 is well recognized for driving vessel growth, lymphatic development, and neuron pathfinding [33]. Outside vascular and neural contexts, NRP2 influences immune processes. As summarized by Schellenburg *et al*., it supports macrophage ripening, dendritic cell stimulation, and T cell maturation and activation [33]. Growing data link NRP2 to macrophage skewing; for instance, in diabetic wounds, FOXM1-triggered M1 polarization relies on the SEMA3C/NRP2/Hedgehog route [34]. Additionally, specific NRP2 variants rise in certain macrophage groups and correlate with engulfment and breast cancer spread [35]. To our awareness, this is the inaugural description of a $CD5L^+$ macrophage group exhibiting heightened clearance in the CRC liver metastatic niche. Accordingly, NRP2's control over $CD5L^+$ macrophage development and programming is newly reported. Still, prior work on NRP2 in standard M1/M2 shifts and macrophage roles offers indirect backing for its wide immune-regulatory scope. Our results thus broaden NRP2 knowledge past typical macrophage categories, emphasizing its fresh involvement in shaping a recently identified clearance-focused macrophage population.

Worth noting, NRP2 serves as a partner receptor for VEGF-C/D, and earlier research has linked the NRP2/VEGF system to tumor advancement via vessel promotion [36, 37]. In our context, hypoxic CRC migrasomes primarily accelerate metastasis by inducing $CD5L^+$ macrophage clearance. Although angiogenic contributions of migrasomes were not probed here, NRP2's known endothelial actions lay the groundwork for upcoming work on potential migrasome effects on tumor vasculature.

Furthermore, this work positions NRP2 as a central player in hypoxic CRC migrasome-triggered macrophage alteration and liver seeding. These insights suggest that blocking NRP2 or interfering with macrophage clearance might curb metastatic advance. Yet, since NRP2 appears in healthy endothelial and lymphatic structures and clearance maintains tissue balance, broad suppression could yield unwanted consequences. Hence, precision approaches, like tumor-directed carriers, are essential. Additional animal models are needed to test the effectiveness and tolerability of NRP2-based treatments in CRC.

Conclusion

Overall, this investigation exposes an undescribed route whereby low-oxygen-triggered migrasomes from CRC foster liver metastasis via NRP2/PROX1-guided reprogramming of $CD5L^+$ macrophages. We illustrate that migrasomes act as transfer agents, delivering NRP2 to target $CD5L^+$ macrophages, thereby boosting their maturation and clearance through PROX1 binding. This effort not only enriches insight into tumor-associated macrophage diversity in CRC but also spotlights the migrasome–NRP2 pathway as a new facilitator of tumor-immune dialogue in metastasis.

Acknowledgments: None

Conflict of Interest: None

Financial Support: None

Ethics Statement: None

References

1. Zhou H, Liu Z, Wang Y, Wen X, Amador EH, Yuan L, et al. Colorectal liver metastasis: molecular mechanism and interventional therapy. Signal Transduct Target Ther. 2022;7:70.
2. Liu QL, Zhou H, Zhou ZG, Chen HN. Colorectal cancer liver metastasis: genomic evolution and crosstalk with the liver microenvironment. Cancer Metastasis Rev. 2023;42:575–87.
3. Zhang X, Yao L, Meng Y, Li B, Yang Y, Gao F. Migrasome: a new functional extracellular vesicle. Cell Death Discov. 2023;9:381.
4. Jiang D, He J, Yu L. The migrasome, an organelle for cell-cell communication. Trends Cell Biol. 2024.
5. Jiang Y, Liu X, Ye J, Ma Y, Mao J, Feng D, et al. Migrasomes, a new mode of intercellular communication. Cell Commun Signal. 2023;21:105.
6. Si M, Wang Q, Li Y, Lin H, Luo D, Zhao W, et al. Inhibition of hyperglycolysis in mesothelial cells prevents peritoneal fibrosis. Sci Transl Med. 2019; 11.
7. Jiao H, Jiang D, Hu X, Du W, Ji L, Yang Y, et al. Mitocytosis, a migrasome-mediated mitochondrial quality-control process. Cell. 2021;184:2896–e29102813.
8. Zhang C, Li T, Yin S, Gao M, He H, Li Y, et al. Monocytes deposit migrasomes to promote embryonic angiogenesis. Nat Cell Biol. 2022;24:1726–38.
9. Jiang D, Jiang Z, Lu D, Wang X, Liang H, Zhang J, et al. Migrasomes provide regional cues for organ morphogenesis during zebrafish gastrulation. Nat Cell Biol. 2019;21:966–77.
10. Jiang D, Jiao L, Li Q, Xie R, Jia H, Wang S, et al. Neutrophil-derived migrasomes are an essential part of the coagulation system. Nat Cell Biol. 2024;26:1110–23.
11. Hu M, Li T, Ma X, Liu S, Li C, Huang Z, et al. Macrophage lineage cells-derived migrasomes activate complement-dependent blood-brain barrier damage in cerebral amyloid angiopathy mouse model. Nat Commun. 2023;14:3945.
12. Lee SY, Choi SH, Kim Y, Ahn HS, Ko YG, Kim K, et al. Migrasomal autophagosomes relieve Endoplasmic reticulum stress in glioblastoma cells. BMC Biol. 2024;22:23.
13. Zhao S, Mi Y, Guan B, Zheng B, Wei P, Gu Y, et al. Tumor-derived Exosomal miR-934 induces macrophage M2 polarization to promote liver metastasis of colorectal cancer. J Hematol Oncol. 2020;13:156.
14. Zhang C, Wang XY, Zhang P, He TC, Han JH, Zhang R, et al. Cancer-derived Exosomal HSPC111 promotes colorectal cancer liver metastasis by reprogramming lipid metabolism in cancer-associated fibroblasts. Cell Death Dis. 2022;13:57.
15. Gu C, Chen P, Tian H, Yang Y, Huang Z, Yan H, et al. Targeting initial tumour-osteoclast spatiotemporal interaction to prevent bone metastasis. Nat Nanotechnol. 2024.
16. Zhang K, Zhu Z, Jia R, Wang NA, Shi M, Wang Y, et al. CD151-enriched migrasomes mediate hepatocellular carcinoma invasion by conditioning cancer cells and promoting angiogenesis. J Exp Clin Cancer Res. 2024;43:160.
17. Huang Y, Luo Y, Ou W, Wang Y, Dong D, Peng X, et al. Exosomal LncRNA SNHG10 derived from colorectal cancer cells suppresses natural killer cell cytotoxicity by upregulating INHBC. Cancer Cell Int. 2021;21:528.
18. Tufan T, Comertpay G, Villani A, Nelson GM, Terekhova M, Kelley S, et al. Rapid unleashing of macrophage efferocytic capacity via transcriptional pause release. Nature. 2024;628:408–15.
19. Mehrotra P, Ravichandran KS. Drugging the efferocytosis process: concepts and opportunities. Nat Rev Drug Discov. 2022;21:601–20.
20. Qiu H, Shao Z, Wen X, Liu Z, Chen Z, Qu D, et al. Efferocytosis: an accomplice of cancer immune escape. Biomed Pharmacother. 2023;167:115540.
21. Werfel TA, Elion DL, Rahman B, Hicks DJ, Sanchez V, Gonzales-Ericsson PI, et al. Treatment-Induced tumor cell apoptosis and secondary necrosis drive tumor progression in the residual tumor microenvironment through MerTK and IDO1. Cancer Res. 2019;79:171–82.
22. Hong SM, Lee AY, Kim BJ, Lee JE, Seon SY, Ha YJ, et al. NAMPT-Driven M2 polarization of Tumor-Associated macrophages leads to an immunosuppressive microenvironment in colorectal cancer. Adv Sci (Weinh). 2024;11:e2303177.

23. Zhou X, Li D, Xia S, Ma X, Li R, Mu Y, et al. RNA-based modulation of macrophage-mediated efferocytosis potentiates antitumor immunity in colorectal cancer. J Control Release. 2024;366:128–41.
24. Gu C, Chen P, Tian H, Yang Y, Huang Z, Yan H, et al. Targeting initial tumour-osteoclast Spatiotemporal interaction to prevent bone metastasis. Nat Nanotechnol. 2024;19:1044–54.
25. Chowdhury M, Das PK. Hypoxia: intriguing feature in cancer cell biology. ChemMedChem. 2024;19:e202300551.
26. Tatrai E, Randelovic I, Surguta SE, Tovari J. Role of hypoxia and Rac1 inhibition in the metastatic cascade. Cancers (Basel). 2024; 16.
27. Guo T, Xu J. Cancer-associated fibroblasts: a versatile mediator in tumor progression, metastasis, and targeted therapy. Cancer Metastasis Rev. 2024;43:1095–116.
28. Liguori M, Digifico E, Vacchini A, Avigni R, Colombo FS, Borroni EM, et al. The soluble glycoprotein NMB (GPNMB) produced by macrophages induces cancer stemness and metastasis via CD44 and IL-33. Cell Mol Immunol. 2021;18:711–22.
29. Bertocchi A, Carloni S, Ravenda PS, Bertalot G, Spadoni I, Lo Cascio A, et al. Gut vascular barrier impairment leads to intestinal bacteria dissemination and colorectal cancer metastasis to liver. Cancer Cell. 2021;39:708–e724711.
30. Rong D, Sun G, Zheng Z, Liu L, Chen X, Wu F, et al. MGP promotes CD8(+) T cell exhaustion by activating the NF-kappaB pathway leading to liver metastasis of colorectal cancer. Int J Biol Sci. 2022;18:2345–61.
31. Zhang R, Peng J, Zhang Y, Zheng K, Chen Y, Liu L, et al. Pancreatic cancer cell-derived migrasomes promote cancer progression by fostering an immunosuppressive tumor microenvironment. Cancer Lett. 2024;605:217289.
32. Hu Q, Chen J, Liu Y, Chen H, Lai H, Jiang L, et al. TSPAN4 + fibroblasts coordinate metastatic niche assembly through migrasome-driven metabolic reprogramming and stromal-immune crosstalk in pancreatic adenocarcinoma. 2025;16–2025.
33. Schellenburg S, Schulz A, Poitz DM, Muders MH. Role of neuropilin-2 in the immune system. Mol Immunol. 2017;90:239–44.
34. Yang Y, Zhang B, Yang Y, Peng B, Ye R. FOXM1 accelerates wound healing in diabetic foot ulcer by inducing M2 macrophage polarization through a mechanism involving SEMA3C/NRP2/Hedgehog signaling. Diabetes Res Clin Pract. 2022;184:109121.
35. Dhupar R, Jones KE, Powers AA, Eisenberg SH, Ding K, Chen F, et al. Isoforms of Neuropilin-2 denote unique Tumor-Associated macrophages in breast cancer. Front Immunol. 2022;13:830169.
36. Benwell CJ, Johnson RT, Taylor J, Price CA, Robinson SD. Endothelial VEGFR coreceptors Neuropilin-1 and Neuropilin-2 are essential for tumor angiogenesis. Cancer Res Commun. 2022;2:1626–40.
37. Dallas NA, Gray MJ, Xia L, Fan F, van Buren G 2nd, Gaur P, et al. Neuropilin-2-mediated tumor growth and angiogenesis in pancreatic adenocarcinoma. Clin Cancer Res. 2008;14:8052–60.